


## Spinor Matter-Wave Control with Nanosecond Spin-Dependent Kicks

Liyang Qiu<sup>1</sup>,\* Lingjing Ji, Jiangyong Hu, Yizun He,<sup>‡</sup> Yuzhuo Wang<sup>1</sup>,<sup>§</sup> and Saijun Wu<sup>†</sup>

*Department of Physics, State Key Laboratory of Surface Physics and Key Laboratory of Micro and Nano Photonic Structures (Ministry of Education), Fudan University, Shanghai 200433, China*

 (Received 19 February 2022; revised 5 May 2022; accepted 9 September 2022; published 3 October 2022)

Significant aspects of advanced quantum technology today rely on rapid control of atomic matterwaves with hyperfine Raman transitions. Unfortunately, efficient Raman excitations are usually accompanied by uncompensated dynamic phases and coherent spin leakages, preventing accurate and repetitive transfer of recoil momentum to large samples. We provide a systematic study to demonstrate that the limitations can be substantially overcome by dynamically programming an adiabatic pulse sequence. Experimentally, counterpropagating frequency-chirped pulses are programmed on an optical delay line to parallelly drive five  $\Delta m = 0$  hyperfine Raman transitions of  $^{85}\text{Rb}$  atoms for spin-dependent kick (SDK) within  $\tau = 40$  ns, with an  $f_{\text{SDK}} \approx 97.6\%$  inferred fidelity. Aided by numerical modeling, we demonstrate that by alternating the chirps of successive pulses in a balanced fashion, accumulation of nonadiabatic errors including the spin leakages can be managed, while the dynamic phases can be robustly cancelled. Operating on a phase-stable delay line, the method supports precise, fast, and flexible control of spinor matterwave with efficient Raman excitations.

DOI: [10.1103/PRXQuantum.3.040301](https://doi.org/10.1103/PRXQuantum.3.040301)

### I. INTRODUCTION

Precise control of effective two-level systems is instrumental to modern quantum technology. In atomic physics, such controllable two-level systems are naturally defined on a pair of long-lived atomic internal states and are often referred to as atomic spins. To control the external motion, quantized photon recoil momentum can be transferred to the atom during spin flips driven by Raman excitations [1–3]. By laser cooling [4], the atomic motion can be sufficiently slowed that the momentum transfers by the rapid optical pulses are effectively instantaneous “spin-dependent kicks” (SDK) [5,6], with the excitation efficiency insensitive to the atomic motion. SDKs are therefore a class of broadband spinor matterwave control techniques with an achievable accuracy similar to those for two-level internal atomic spin controls [7–9]. Beyond traditional applications such as to enhance the enclosed area of light-pulse atom interferometers [3,6,10], SDKs

emerge as an important technique to control spin-motion entanglement and to improve the scalability of ion-based quantum information processing [5,11–13].

For precise spinor matterwave control, it is essential to operate SDK at high enough speed to suppress low-frequency noises and to compose multiple operations within a limited duration. Furthermore, except for working with microscopically confined samples [5,8,13], high-quality optical control needs to be highly resilient to intensity errors associated with illumination inhomogeneity [14,15]. To meet the fidelity requirements by the next-generation quantum technology [16–21], particularly for large samples, high-speed implementation of error-resilient composite techniques [22–24] are likely required. However, the SDK speed is practically limited by intricate requirements associated with precise Raman control, including the following two categories.

The first type of SDK speed constraint is associated with multilevel dynamics accompanying the Raman control of “real” atoms. To avoid spontaneous emission, the Raman excitation bandwidth has to be much smaller than the single-photon detuning  $\Delta_e$  [Fig. 1(a)] to avoid populating the excited states. But a moderate  $\Delta_e$  is typically required for efficient control with limited laser power, as well as for managing the differential Stark shifts [Fig. 1(b)] [25]. In addition, as to be clarified further, to avoid the  $m$ -changing transitions during Raman excitation [26], one usually lifts the Zeeman degeneracy with a strong enough quantization field [27]. The typically moderate field strength also limits the speed of the Raman control.

\*lyqiu16@fudan.edu.cn

†saijunwu@fudan.edu.cn

‡Current address: Research Department, Hisilicon, Huawei, Shenzhen 518129, China.

§Current address: Institute of Laser Spectroscopy, Shanxi University, Taiyuan, 030006, China.

*Published by the American Physical Society under the terms of the [Creative Commons Attribution 4.0 International](https://creativecommons.org/licenses/by/4.0/) license. Further distribution of this work must maintain attribution to the author(s) and the published article’s title, journal citation, and DOI.*

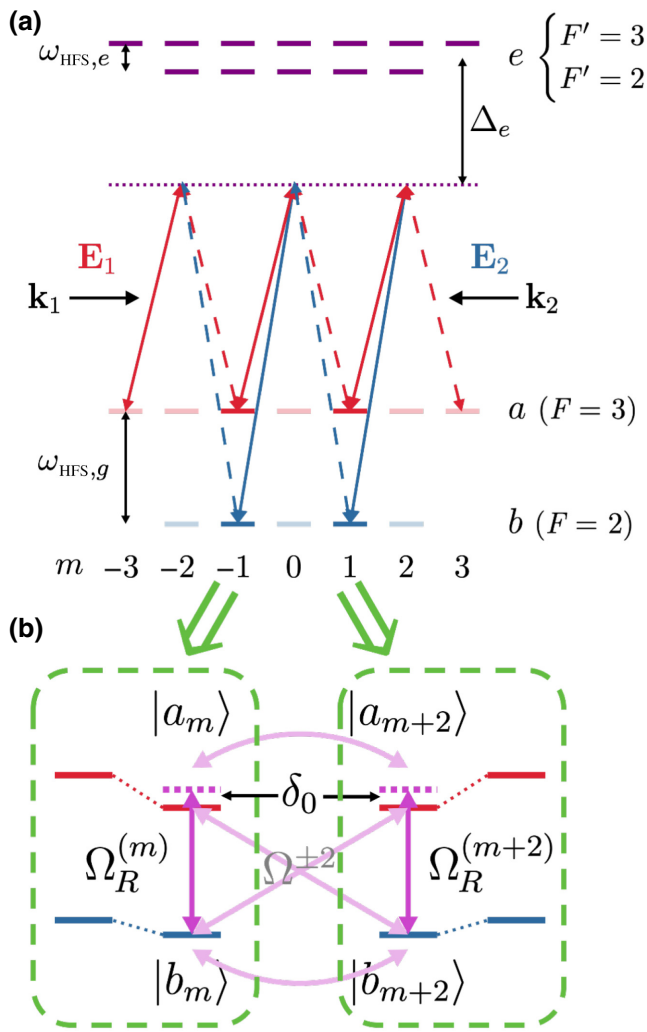


FIG. 1. Schematic of SDK on a hyperfine manifold, with the  $^{85}\text{Rb}$  D1 line as the example in this work. (a) Cross-linearly polarized, counterpropagating  $\mathbf{E}_{1,2}$  resonantly drive the  $\Delta m = 0$  and  $\Delta m = \pm 2$  Raman transitions. The optical couplings are illustrated with solid and dashed lines, with  $m = \pm 1, \pm 3$  ground states as examples. When the single-photon detuning  $\Delta_e$  is much larger than the excited state hyperfine splitting  $\omega_{\text{HFS},e}$ , the  $\Delta m = \pm 2$  couplings through the  $F' = 2, 3$  intermediate states largely cancel each other, leading to decoupled  $\{|a_m\rangle, |b_m\rangle\}$  subspin systems. (b) The reduced level diagrams for the weakly coupled  $\{|a_m\rangle, |b_m\rangle\}$  systems ( $m = \pm 1$ ). The bare levels are relatively shifted and Raman coupled. The effective Hamiltonian parameters  $\Omega^{\pm 2}$ ,  $\Omega_R^{(m)}$ ,  $\delta_0$  for Eqs. (1) (2) (3) are marked. The differential Stark shift  $\delta_0$  is largely responsible for the SDK dynamic phase [Eq. (5)]. Similarly coupled subspin systems composed of  $\{|a_m\rangle, |b_m\rangle\}$  with  $m = 0, \pm 2$  are not shown.

The second type of SDK speed constraint is associated with the requirement of controllable direction of the recoil momentum transfer. As in Fig. 1, when counterpropagating  $\mathbf{E}_{1,2}$  pulses are applied to drive a Raman transition, to ensure the preference for the atom to absorb a photon from the  $\mathbf{E}_1$  field followed by a stimulated emission into the

$\mathbf{E}_2$  field, a certain mechanism is needed to prevent the time-reversed Raman process from occurring. For hyperfine spin control of alkalinelike atoms, the directionality is ultimately supported by the ground-state hyperfine splitting  $\omega_{\text{HFS},g}$  [5]. Practically, however, when the Raman interferometry is operated in the retroreflection geometry with established advantages [28–33], the directionality is typically protected by the moderate two-photon frequency differences introduced either by additional frequency modulations [3,28] or Doppler shifts of moving atoms [29], which in turn limit the SDK speed.

The purpose of this work is to improve the speed and precision of spinor matterwave control in the presence of the aforementioned technical barriers. In particular, we study Raman adiabatic SDK [6,10] within nanoseconds in a retroreflection optical setup [32,34], for alkaline atoms with Zeeman degeneracy prone to coherent spin leakage. As schematically summarized in Fig. 1 (level diagram) and Fig. 2 (experimental implementation), counterpropagating frequency-chirped pulses are programmed on the optical delay line to adiabatically drive the  $F_b = 2 \leftrightarrow F_a = 3$  Raman transitions of  $^{85}\text{Rb}$  through the D1 line, while imparting  $\pm \hbar \mathbf{k}_R$  momentum “kicks” to atoms. Here  $\mathbf{k}_R = \mathbf{k}_2 - \mathbf{k}_1$  is the difference of  $\mathbf{k}$  vectors between the pulse pair. The adiabatic Raman transfer technique [6,10,35] [Figs. 2(b) and 2(c)] provides the intensity-error resilience for the focused laser to address a mesoscopic sample. To enforce the directionality in the standard retroreflection geometry [32,34], the regular method of resolving the two-photon frequency differences [3,28,29] are abandoned. Instead, we exploit the fact that the nanosecond pulses are short enough to be spatially separated [Fig. 2(a)], allowing controllable collision of specific Raman pulses within the atomic sample, at specific instances, to drive the Raman transitions.

Experimentally, equipped with a wideband optical arbitrary waveform generation system (OAWG) [36], we drive adiabatic SDKs within tens of nanoseconds, the fastest realization to date [6,10], by shaping counterpropagating pulses (Fig. 2) with merely tens of milliwatts laser power. The spin population and momentum transfer are measured and compared with full-level numerical simulations, with which we infer a SDK fidelity of  $f_{\text{SDK}} \approx 97.6(3)\%$ . The  $\delta f \sim 2.5\%$  infidelity, as unveiled by the full-level numerical simulation, is primarily limited by spontaneous emission and the  $\Delta m = \pm 2$  leakage among Zeeman sublevels within the ground-state hyperfine manifold [Fig. 1(b)] at the moderate  $\Delta_e = 2\pi \times 10$  GHz detuning.

Aided by numerical modeling, we further demonstrate that beyond the incoherent momentum and population transfer, high-fidelity spinor matterwave “phase gates” capable of coherently transferring many recoil momenta can be synthesized by nanosecond adiabatic SDKs on the delay line. This is despite the coherent spin leakage and intensity-dependent diffraction phase

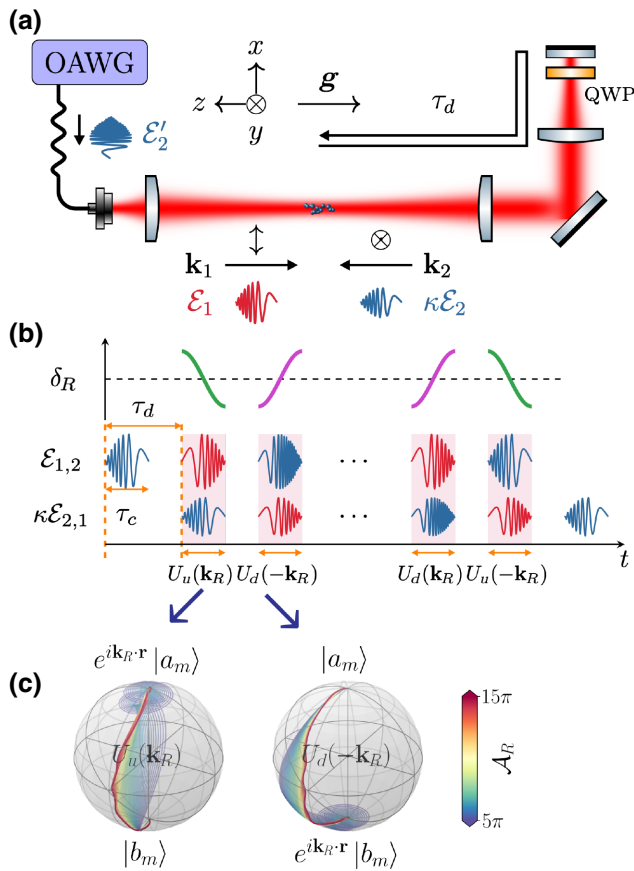


FIG. 2. (a) Schematic setup. Frequency-chirped optical waveforms [illustrated with the real part of the complex envelope function  $\mathcal{E}_{1,2}$ , sharing the same color coding as those for  $\mathbf{E}_{1,2}$  in Fig. 1(a)] are programmed by an optical arbitrary waveform generator (OAWG) and sent through a single-mode fiber to the delay line. An  $\mathbf{E}_1$  pulse collides with a retroreflected  $\mathbf{E}_2$  pulse at the atomic sample to drive the  $|a_m\rangle \leftrightarrow |b_m\rangle$  Raman transition while imparting  $\pm\hbar\mathbf{k}_R$  kicks to atoms reaching  $|a_m\rangle$  and  $|b_m\rangle$ , respectively. Next, after a delay time  $\tau_d$ , the  $\mathbf{E}_1$  pulse is retroreflected to meet  $\mathbf{E}'_2$  at the same location to further boost the  $|a_m\rangle, |b_m\rangle$  separation. QWP, quarter-wave plate. (b) The timing sequence for the “balanced chirp-alternating scheme” [Eq. (11)]. The two-photon detunings  $\delta_R$  are plotted versus time. The adiabatic controls with “up-chirp” and “down-chirp” two-photon detuning  $\delta_R$  are referred to as  $U_u$  and  $U_d$ , respectively. Here the amplitudes for the retroreflected pulses are reduced by a  $\kappa$  factor. Typical Bloch-sphere dynamics of an  $\{|a_m\rangle, |b_m\rangle\}$  spinor ( $m = 0$ ) are given in (c) at various laser intensities parametrized by the Raman pulse area  $\mathcal{A}_R$ . The weak  $\Delta m = \pm 2$  couplings [Fig. 1(b), Eq. (1)] are ignored.

broadening [6,25,37,38] by individual “kicks,” at the moderate  $\Delta_e$  [8,39]. In particular, we demonstrate that a tailored adiabatic sequence with alternating up and down two-photon chirps [40] [Figs. 2(b) and 2(c)] suppresses the coherent accumulation of spin leakages across the nearly degenerate hyperfine levels dressed by the cross-linearly polarized pulses [Fig. 1(b)]. Furthermore, as to be clarified further, the time-reversal symmetry of the chirp-balanced

scheme ensures robust cancellation of the dynamic, laser intensity-dependent diffraction phases, with  $\Delta_e > \omega_{\text{HFS},g}$  unbounded by traditional choices [25,41], even in the presence of nonperfect retroreflection [Fig. 2(b)] [32].

Our work suggests that fast, large-momentum atom optics can be synthesized for accurately manipulating multilevel atoms in the unconventional regime of Raman control [25,41]. Comparing with atom interferometric large-momentum beam-splitting techniques based on high-order Bragg diffraction [42,43], Bloch oscillations [44,45], as well as traditional Raman schemes [3,6,10], the key advantage offered by our SDK technique is the ultrahigh SU(2) operation speed. The high speed not only helps the composite technique to avoid the complexity of continuous motion itself, but also protects the precise intensity-error cancellation in the presence of low-frequency noises, including those due to atomic motion in inhomogeneous laser beams. We notice that similar advantages are shared by the recently developed high-speed clock atom interferometry [46,47], where the atomic spins are defined directly on kHz-level optical lines, to achieve exceptionally high momentum transfer efficiencies. Similar to that technique, to coherently drive the hyperfine spins within nanoseconds requires high laser intensities. The nanosecond SDK in this work is realized by weakly focusing the milliwatt-level pulses to a mesoscopic sample. To address larger samples for, e.g., inertial sensing [34,43] on a compact delay line, more advanced laser modulation techniques need to be developed for generating high-power wideband optical waveforms.

In the following the main part of the paper is structured into three sections. In Sec. II, we set up a light-atom interaction framework where multilevel couplings are treated as perturbations to the effective two-level Raman interaction within the ground-state hyperfine manifold. Key notations and quantities for the experimental and numerical studies are defined. In Sec. III, we demonstrate the flexible matter-wave control by programming counterpropagating pulses on an optical delay line with OAWG [36]. Constrained by experimental resources, the characterization of the adiabatic SDK technique is limited to the inference of the SDK fidelity with atomic velocity and hyperfine population measurements. However, in Sec. IV, we demonstrate efficient suppression of coherent spin-leakage accumulation and intensity-dependent dynamic phases by the chirp-balanced SDK scheme and provide numerical evidence that the chirp-balanced SDK scheme supports coherently control of multispinor matterwave with large momentum transfer, even with a moderate laser power in the 10 mW range as in this work.

## II. THEORETICAL MODEL

### A. Spin-dependent kicks on a hyperfine manifold

We consider Fig. 1(a) alkalinelike atom subjected to Raman excitation on the D1 line. Similar

conclusions hold for D2 excitations. The Zeeman-degenerate  $a, b$ , and  $e$  hyperfine states with total angular momentum  $F_{a,b}$  and  $F'_e$  are labeled as  $|c_m\rangle \equiv |c, F_c, m\rangle$  with magnetic quantum number  $m \in [-F_c, F_c]$ . Here, with the nuclear spin  $I > 1/2$ , there are  $2F_c + 1$  Zeeman sublevels for each manifold  $c \in \{a, b\}$ , and similarly for the  $e$  manifold. The  $|a_m\rangle \leftrightarrow |b_n\rangle$  hyperfine Raman transition is driven by pairs of counterpropagating laser pulses,  $\mathbf{E}_{1,2} = \mathbf{e}_{1,2} \mathcal{E}_{1,2} e^{i(\mathbf{k}_{1,2} \cdot \mathbf{r} - \omega_{1,2} t)} + \text{c.c.}$  with shaped slowly varying amplitudes  $\mathcal{E}_{1,2}(\mathbf{r}, t)$  and Raman-resonant carrier-frequency difference  $\omega_2 - \omega_1 = \omega_{\text{HFS},g}$ .

Although motion of the multilevel atom in the pulsed  $\mathbf{E}_{1,2}$  fields is quite complicated (Appendix A), the internal state dynamics can be substantially simplified when the laser polarization  $\mathbf{e}_{1,2}$  are chosen to be cross-linear [Fig. 2(a)] [30,31] and the single-photon detuning  $\Delta_e$  is much larger than the excited-state hyperfine splitting  $\omega_{\text{HFS},e}$ . In this case, the destructive interference of Raman couplings through the intermediate  $|e_l\rangle$  levels prevent efficient  $\Delta m = \pm 2$  transitions [the rule in Fig. 1(a) is that efficient Raman couplings are only composed by pairs of dipole couplings drawn with the same type of solid or dashed lines] [26]. The residual “leaking” Raman Rabi frequency [Fig. 1(b)] scales as

$$\Omega^{\pm 2} = \mathcal{O}\left(\frac{\omega_{\text{HFS},e}}{\Delta_e}\right) \Omega_R, \quad (1)$$

with  $\Omega_R = \Omega_a^{1*} \Omega_b^2 / 2\Delta_e$ ,  $\Omega_{a(b)}^{1(2)} = \frac{\mathcal{E}_{1(2)}}{\hbar} \frac{1}{\sqrt{3}} |\langle J_g || \mathbf{d} || J_e \rangle|$  [48].

Therefore, in the large  $\Delta_e$  limit, the Raman dynamics in the ground-state manifold is decomposed into those within  $2F_b + 1$  copies of pseudo spin-1/2 subspaces  $\{|a_m\rangle, |b_m\rangle\}$ , labeled by magnetic quantum number  $m$  [see Fig. 1(b) for the  $m = \pm 1$  examples]. For each  $m$  spin, the Rabi frequency driven by the Raman pulse can be written as

$$\Omega_R^{(m)} = \chi^{(m)} \Omega_R. \quad (2)$$

The close-to-unity factor  $\chi^{(m)}$  is determined by the associated Clebsch-Gordan coefficients, normalized at  $\chi^{(0)} = 1$  and decreases slowly with  $|m|$  [49]. The Hamiltonian for the  $m$  spin is given by

$$H_0^{(m)}(\mathbf{r}, t) = \hbar \left( \frac{\delta_0}{2} \sigma_z^{(m)} + \frac{\Omega_R^{(m)}}{2} e^{i\mathbf{k}_R \cdot \mathbf{r}} \sigma_+^{(m)} + \text{h.c.} \right). \quad (3)$$

Here the detuning  $\delta_0$  is the ( $m$ -independent) differential Stark shift between the two hyperfine ground states that can be nullified at suitable  $\Delta_e/\omega_{\text{HFS},g}$  and  $\Omega_{a,b}$  combinations [25]. The Pauli matrices  $\{\sigma_x^{(m)}, \sigma_y^{(m)}, \sigma_z^{(m)}\}$  are defined by  $\sigma_+^{(m)} \equiv \sigma^{a_m b_m}$  [50]. For notation convenience in the following, we further define projection operators  $\mathbf{1}^{(m)} \equiv \sigma^{a_m a_m} + \sigma^{b_m b_m}$  and  $\bar{\mathbf{1}}^{(m)} = 1 - \mathbf{1}^{(m)}$ , respectively.

With the major part of the resonant Raman interaction identified, the D1 multilevel dynamics [Fig. 1(a)] governed by the effective light-atom interaction Hamiltonian, as detailed in Appendix A, can be written as

$$H_{\text{eff}}(\mathbf{r}, t) = \sum_{m=-F_b}^{F_b} H_0^{(m)}(\mathbf{r}, t) + V'(\mathbf{r}, t) \quad (4)$$

to describe the Raman-dressed ground-state dynamics. Apart from the  $\Delta m = \pm 2$  couplings specified by Eq. (1), the  $V'$  term includes non-Hermitian and nonadiabatic  $|e_l\rangle$  couplings, the  $m$ -sensitive light shifts [26], and the “counter-rotating” couplings involving detuned Raman excitations [Eq. (A3)].

With the atomic position  $\mathbf{r}$  parameter in Eq. (4) as a quantum mechanical operator acting on the external atomic wave function, the Eq. (4) Hamiltonian can propagate the spinor matterwave together with the kinetic  $\hat{P}^2/2M$  operator, see Appendix B for implementation ( $\hat{P} = i\hbar\nabla$  and  $M$  the atomic mass). During nanosecond intervals, however, the matterwave dispersion for the laser-cooled atoms is negligibly small. It is therefore possible to design broadband matterwave controls for iterative applications. In particular, a spin-dependent kick is a transfer of photon momentum to atoms accompanied by a spin flip [5,6]. We refer an ideal SDK as

$$U_K(\mathbf{k}_R) = \prod_{m=-F_b}^{F_b} \left( e^{i\varphi^+} e^{i\mathbf{k}_R \cdot \mathbf{r}} \sigma_+^{(m)} - \text{h.c.} + \bar{\mathbf{1}}^{(m)} \right). \quad (5)$$

The  $\varphi^+$  is a diffraction phase offset [51], which is generally Zeeman state  $m$  and laser intensity  $|\mathcal{E}|^2$  dependent.

In the following our goal is to construct perfect  $U_K(\mathbf{k}_R)$  operation as in Eq. (5) from the full Hamiltonian in Eq. (4), and furthermore to design multiple SDKs with suppressed  $m$  and  $|\mathcal{E}|^2$  dependence. For the purpose, we first define a fidelity  $f_{\text{SDK}}$  to qualify the implementation.

## B. Nonideal SDK

To qualify Fig. 2 SDK implementation modeled by the Eq. (4) Hamiltonian, we refer the imperfect realization of SDK as  $\tilde{U}(\mathbf{k}_R; \eta)$  with  $\eta$  to generally represent relevant Hamiltonian parameters. We define an average fidelity [52] over the whole atomic ensemble for a single SDK acting on the  $\{|b_m\rangle\}, \{|a_m\rangle\}$  states as

$$f_{\text{SDK}} = \left\langle \left| \left\langle c_m | U_K^\dagger(\mathbf{k}_R) \tilde{U}(\mathbf{k}_R; \eta) | c_m \right\rangle \right|_z^2 \right\rangle_{\eta, c_m}. \quad (6)$$

Here the  $\tilde{U}(\mathbf{k}_R; \eta) | c_m \rangle$  is compared to  $U_K(\mathbf{k}_R) | c_m \rangle$  across the atomic sample with an  $\langle \dots \rangle_z$  average. An ensemble average of the mode-squared fidelity is then performed

with  $\langle \dots \rangle_\eta$  over the Hamiltonian parameters of interest. Assuming light intensity hardly varies along  $z$  over the wavelength-scale distance of interest [Fig. 2(a)], the SDK fidelity defined in this way becomes insensitive to the diffraction phase  $\varphi^+$  and therefore provides a convenient measure for the quality of controlling incoherent observables, such as for the recoil momentum and hyperfine population transfer to be experimentally measured next. The  $\langle \dots \rangle_{c_m}$  instead performs the average over the  $2(2F_b + 1)$  initial states of interest with  $m = -F_b, \dots, F_b$  and  $c = a, b$ .

To quantify the leakage of an atomic state out of each spin subspace  $\{|a_m\rangle, |b_m\rangle\}$  by  $V^r(\mathbf{r}, t)$ , we define an average spin-leakage probability by the nonideal SDK as

$$\varepsilon_{\text{leak}} = 1 - \langle \langle c_m | \tilde{U}^\dagger(\mathbf{k}_R, \eta) \mathbf{1}^{(m)} \tilde{U}(\mathbf{k}_R; \eta) | c_m \rangle \rangle_{\eta, c_m}. \quad (7)$$

By comparing Eq. (6) with Eq. (7) it is easy to verify  $f_{\text{SDK}} \leq 1 - \varepsilon_{\text{leak}}$ , that is, any spin leakage leads to inefficient control. The leakage probability  $\varepsilon_{\text{leak}}$  by Eq. (7) includes contributions from  $\Delta m = \pm 2$  transition as well as those due to spontaneous emission, as  $\varepsilon_{\text{leak}} = \varepsilon_{\Delta m} + \varepsilon_{\text{sp}}$ . Here the spontaneous emission probability  $\varepsilon_{\text{sp}}$  during the SDK control is obtained by evaluating  $\tilde{U}(\mathbf{k}_R; \eta)$  with the stochastic wave-function method [53,54] (Appendix B). For the  $\Delta m = \pm 2$  leakage, we find  $\varepsilon_{\Delta m} \propto \omega_{\text{HFS},e}^2 / \Delta_e^2$ , as by Eq. (1), and is thus suppressible at large  $\Delta_e$  similar to the suppression of spontaneous emission. However, one should note that unlike spontaneous emission, which simply leads to decoherence, the  $\Delta m = \pm 2$  leakage is a coherent process. A sequence of such coherent leakages may quickly add up in amplitudes to become significant, even if  $\varepsilon_{\Delta m}$  for a single SDK is negligibly small.

### C. Adiabatic SDK

To achieve a uniformly high SDK fidelity across an intensity-varying sample volume, particularly for  $m$  spin on a hyperfine manifold with different  $\Omega_R^{(m)}$  [Fig. 1, Eq. (2)], a standard technique is to exploit the geometric robustness of two-level system by inducing an adiabatic rapid passage [Fig. 2(a)] [6,10,35,55,56]. For a particular  $\{|a_m\rangle, |b_m\rangle\}$  subspin, if we ignore  $V^r$  in Eq. (4), then the Raman adiabatic passage can easily be generated by the  $H_0^{(m)}$  Hamiltonian. In particular, we parametrize the Rabi frequency of the two pulses as  $\Omega_{a(b)}^{1(2)} = C_{a(b)} e^{i\phi_{1(2)}}$ , and specifically consider the time-dependent phase difference and the amplitude profile as  $\Delta\phi(t) = \phi_0 \sin(\pi t / \tau_c)$ ,  $C_{a(b)}(t) = C_{a(b)}^{(0)} \sin(\pi t / \tau_c)$ , respectively, for  $t \in [0, \tau_c]$  [Fig. 3(b) inset]. With a large enough two-photon sweep frequency  $\delta_{\text{swp}} = \pi \phi_0 / \tau_c$ ,  $|\delta_{\text{swp}}| \gg \delta_0$  to let the two-photon detuning  $\delta_R = \Delta\phi$  cover the differential Stark shift  $\delta_0$  [Fig. 2(b)], a strong enough Raman Rabi amplitude  $C_R^{(0)} = C_a^{(0)} C_b^{(0)} / 2\Delta_e = 2\chi^{(m)} \mathcal{A}_R / \tau_c$  with a

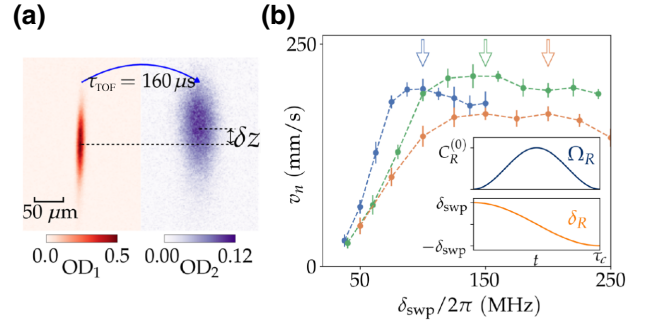


FIG. 3. (a) SDK momentum transfer measurement with a double imaging method: for atomic sample subjecting  $n$  SDKs ( $n = 25$  here) starting with  $\tilde{U}_u(\mathbf{k}_R)\tilde{U}_u(-\mathbf{k}_R)$ , a sequence of two absorption images are taken at  $\bar{t}_1 = 10 \mu\text{s}$  and  $\bar{t}_2 = \bar{t}_1 + t_{\text{TOF}}$ , separated by  $\tau_{\text{TOF}} = 160 \mu\text{s}$  time of flight and with a hyperfine repumping pulse along  $x$  applied in between (see main text). The center-of-mass position shift  $\delta z$  is retrieved with a typical  $\pm 2 \mu\text{m}$  accuracy by fitting the optical depth (OD). The recoil velocity  $v_n = \delta z / \tau_{\text{TOF}}$  is then estimated during typical adiabatic SDK parameter scan as in (b). Here, with  $n = 25$ ,  $\tau_c = 60 \text{ ns}$  SDK pulses applied,  $v_n$  is optimized as a function of sweep frequency  $\delta_{\text{swp}}$ , and peak laser intensity parametrized by an estimated peak Raman pulse area  $\mathcal{A}_R = C_R^{(0)} \tau_c / 2$ . Blue, green, and orange lines correspond to estimated peak  $\mathcal{A}_R$  of approximately  $6\pi$ ,  $9\pi$ ,  $12\pi$ , respectively. The corresponding peak Rabi frequencies  $C_R^{(0)}$  are marked with arrows on the top along the  $\delta_{\text{swp}}$  axis. The error bars give statistical uncertainties of  $v_n$  in repeated measurements.

peak Raman pulse area  $\mathcal{A}_R \gg 1$ , and matched magnitudes between  $C_R^{(0)}$  and  $\delta_{\text{swp}}$ , SDK can be generated in a quasia-adiabatic manner [57,58], i.e., with atomic state  $|\psi_m(t)\rangle \approx c_a(0)e^{i\varphi_a(t)}|\tilde{a}_m(t)\rangle + c_b(0)e^{i\varphi_b(t)}|\tilde{b}_m(t)\rangle$  following the adiabatic basis  $\{|\tilde{a}_m(t)\rangle, |\tilde{b}_m(t)\rangle\}$ , which are simply the eigenstates of the instantaneous Hamiltonian. Population inversion are thus driven quasia-adiabatically during  $0 < t < \tau_c$  with the efficiency insensitive to the laser intensity, detuning, and their slow deviations from the specific time-dependent forms. Putting back the  $\mathbf{r}$  dependence, the diffraction phase accompanying the population inversion,  $\tilde{\varphi}^+(\mathbf{r}) \equiv \tilde{\varphi}^+ + \mathbf{k}_R \cdot \mathbf{r}$ , is evaluated as  $\tilde{\varphi}^+(\mathbf{r}) = \varphi_a(\tau_c) - \varphi_b(\tau_c)$ , which includes not only a geometric phase  $\varphi_G = \pi/2 + \mathbf{k}_R \cdot \mathbf{r}$  [59,60], but also a dynamic phase  $\varphi_{D,m} \propto \int_0^{\tau_c} (\langle \tilde{a}_m | H_0^{(m)} | \tilde{a}_m \rangle - \langle \tilde{b}_m | H_0^{(m)} | \tilde{b}_m \rangle) d\tau$  sensitive to the control parameters  $\Omega_{a(b)}^{1(2)}$  characterized by the laser intensity profiles.

### D. Dynamic phase cancellation

The  $U_K(\mathbf{k}_R)$  operation [Eq. (5)] prints matterwave with state  $m$ - and laser intensity  $|\mathcal{E}|^2$ -dependent diffraction phases  $\varphi^+$  in general. For interferometrically useful coherent matterwave controls, these dynamic parts of  $\varphi^+$  need to be suppressed. It is worth noting that the dynamic phase for the adiabatic SDK survives at vanishing  $\delta_0$  [25,60]. Therefore, coherent matterwave control with

adiabatic SDK requires certain dynamic phase cancellation in general.

The dynamic phases for perfect SDKs can be cancelled in pairs. To avoid trivial operations during the pairing, the two-photon wave vector  $\mathbf{k}_R$  can be inverted [3,6,10], leading to

$$U_K^{(2N)}(\mathbf{k}_R) = \underbrace{U_K(-\mathbf{k}_R)U_K(\mathbf{k}_R) \cdots U_K(-\mathbf{k}_R)U_K(\mathbf{k}_R)}_{2N} \\ = \prod_{m=-F_b}^{F_b} \left( (-1)^N e^{i2N\mathbf{k}_R \cdot \mathbf{r}\sigma_z^{(m)}} + \bar{\mathbf{1}}^{(m)} \right). \quad (8)$$

Within each  $m$ -spin space span by  $\{|a_m\rangle, |b_m\rangle\}$ , the  $U_K^{(2N)}(\mathbf{k}_R)$  acts as a position-dependent phase gate to pattern the two components of arbitrary spinor matterwave with  $\pm(2N\mathbf{k}_R \cdot \mathbf{r})$  phases, i.e., to coherently transfer opposite photon recoil momenta to the spin components.

Practically, however, swapping the  $\mathbf{k}$  vectors of  $\mathbf{E}_{1,2}$  can affect other pulse parameters [28,29,32,61]. Here, the  $\mathbf{k}$ -vector swapping is achieved on the delay line with retroreflection (Fig. 2) by programming the carrier frequencies  $\omega_1 \leftrightarrow \omega_2$  for the delayed pulses. The imperfect reflection with  $\kappa < 1$  generally leads to unbalanced diffraction phases [34]  $\tilde{\varphi}^+$  associated with  $\tilde{U}(\pm\mathbf{k}_R)$ . For the spinor matterwave control, we quantify the impact of dynamic phase by comparing the phase of imperfectly controlled  $\tilde{U}^{(2N)}|c_m\rangle$  with the ideal  $U_K^{(2N)}|c_m\rangle$  ( $c = a, b$ ),

$$\varphi_{D,m}^{(2N)} = \arg[\langle a_m | U_K^{(2N)\dagger}(\mathbf{k}_R) \tilde{U}^{(2N)}(\mathbf{k}_R; \eta) | a_m \rangle] \\ - \arg[\langle b_m | U_K^{(2N)\dagger}(\mathbf{k}_R) \tilde{U}^{(2N)}(\mathbf{k}_R; \eta) | b_m \rangle]. \quad (9)$$

### E. Chirp-alternating adiabatic SDK schemes

A central goal of this work is to synthesize perfect  $U_K^{(2N)}(\mathbf{k}_R)$  spinor matterwave phase gates with  $2N$  imperfect  $\tilde{U}(\pm\mathbf{k}_R)$ , even in the presence of the unbalanced dynamic phase  $\varphi_{D,m}^{(2N)}$  and the  $\Delta m = \pm 2$  leakage. For this purpose, we refer the experimentally realized nonideal adiabatic SDKs with an equal amount of positive ( $\delta_{\text{swp}} > 0$ ) and negative ( $\delta_{\text{swp}} < 0$ ) two-photon sweeps as  $\tilde{U}_u(\pm\mathbf{k}_R)$  and  $\tilde{U}_d(\pm\mathbf{k}_R)$ , respectively [Fig. 2(b)]. The associated control Hamiltonians are  $H_u(\mathbf{r}, t)$  and  $H_d(\mathbf{r}, t)$ . In Sec. IV C we show that a chirp-alternating sequence

$$\tilde{U}_{ud}^{(2N)}(\mathbf{k}_R) = \underbrace{\tilde{U}_u(-\mathbf{k}_R)\tilde{U}_d(\mathbf{k}_R) \cdots \tilde{U}_u(-\mathbf{k}_R)\tilde{U}_d(\mathbf{k}_R)}_{2N}, \quad (10)$$

fairly efficiently suppresses the  $\Delta m = \pm 2$  leakage. Next, as detailed in Secs. IV C, IV D, by combining the  $\tilde{U}_{ud}^{(2N)}$

and  $\tilde{U}_{du}^{(2N)}$  to form a balanced chirp-alternating sequence,

$$\tilde{U}_{uddu}^{(4N)}(\mathbf{k}_R) = \tilde{U}_{ud}^{(2N)}(\mathbf{k}_R)\tilde{U}_{du}^{(2N)}(\mathbf{k}_R), \quad (11)$$

the dynamic phases by  $\tilde{U}_{du}^{(2N)}(\mathbf{k}_R)$  and  $\tilde{U}_{ud}^{(2N)}(\mathbf{k}_R)$  robustly cancel each other. The Eq. (11) scheme can therefore faithfully realize a  $U_K^{(4N)}(\mathbf{k}_R)$  phase gate.

For comparison, here the ‘‘traditional’’ chirp-repeating sequences [6,10,62] are defined as

$$\tilde{U}_{uu}^{(2N)}(\mathbf{k}_R) = \underbrace{\tilde{U}_u(-\mathbf{k}_R)\tilde{U}_u(\mathbf{k}_R) \cdots \tilde{U}_u(-\mathbf{k}_R)\tilde{U}_u(\mathbf{k}_R)}_{2N}. \quad (12)$$

Similar  $\tilde{U}_{dd}^{(2N)}(\mathbf{k}_R)$  controls are defined with  $u \rightarrow d$  replacements.

To conclude this section, we note that while the D1 line is chosen in this work (Fig. 1), the conclusions on the ground-state hyperfine dynamics can be applied in a straightforward manner to the D2 line. Comparing with the D1 operation, Raman SDK at the same single-photon detuning  $\Delta_e$  on the D2 line suffers more spontaneous emission loss due to the excitations of the cycling transitions [63]. On the other hand, a reduced  $m$ -changing rate [Eq. (1)] is expected to help the D2 performance due to the typically smaller  $\omega_{\text{HFS},e}$  for the intermediate  $P_{3/2}$  states.

## III. EXPERIMENTAL IMPLEMENTATION

### A. Nanosecond SDK on a delay line

The adiabatic SDK is implemented on the  $^{85}\text{Rb}$   $5S_{1/2} - 5P_{1/2}$  D1 line as depicted in Fig. 1, with counterpropagating chirp pulses programmed by a wideband optical waveform generator [36] on an optical delay line [15]. The cross-linear polarization is realized by double passing the light beam with a quarter-wave plate before the end mirror [Fig. 2(a)], which converts the incident  $\mathbf{e}_x$  polarization to  $\mathbf{e}_y$ . With the OAWG output peak power limited to  $P_{\text{max}} \approx 20$  mW, the incident control pulse  $\mathcal{E}_{1,2}$  is weakly focused to a waist radius of  $w \approx 13$   $\mu\text{m}$  to reach a peak Rabi frequency of  $\Omega_{a(b)} \approx 2\pi \times 2$  GHz. The imperfect retroreflection with  $\kappa \approx 0.7$  ( $r = |\kappa|^2 \approx 50\%$ ) reflectivity, primarily limited by increased focal beam size due to wave-front distortion, leads to decreased  $\Omega_{b(a)} = \kappa\Omega_{b(a)}$  for the reflected pulses seen by the atomic sample. We set the single-photon detuning to be  $\Delta_e = 2\pi \times 10$  GHz to achieve a peak Raman Rabi frequency of  $C_R^{(0)} \approx 2\pi \times \kappa 300$  MHz estimated at the center of the Gaussian  $\mathcal{E}_{1,2}$  beams. An  $\tau_d = 140.37$  ns optical delay is introduced by the  $L \approx 20$  m folded delay line, which is long enough to spatially resolve the counter-propagating nanosecond pulses. To form the counterpropagating  $\mathcal{E}_{1,2}$  pulse pair, we preprogram  $\mathcal{E}_{1,2}(t)$  and  $\mathcal{E}_{2,1}(t - \tau_d)$ , with a relative delay matching the optical delay line, to ensure

the pulse pair with proper carrier frequency  $\omega_{1,2}$  meeting head on head in the atomic cloud. To continue multiple SDKs, additional, individually shaped pulses with alternating  $\omega_{1,2}$  can be applied, as in Fig. 2(b), with a  $T_{\text{rep}} = \tau_d$  periodicity.

Importantly, to periodically generate multiple Raman SDKs with the delay line, every shaped pulse contributes twice to the SDK sequence. To properly shape the Raman coupling  $\Omega_R(t) \propto \mathcal{E}_1^*(t)\mathcal{E}_2(t)$  [Eq. (2)], therefore, one needs to program the incident  $\mathcal{E}'_{1(2)}$  pulse according to the retroreflected  $\mathcal{E}_{2(1)}$  pulse. To clear out such pulse-history dependence in a long sequence, the retroreflection cycles can be interrupted a few times by increasing the interpulse delays beyond  $\tau_d$ . Here, if our goal is to alternate Raman chirps  $\delta_R$ , as in Fig. 2(b) and Eq. (11), then the frequency-sweeping amplitudes for every other incoming optical pulse needs to be increased by an additional  $\delta_{\text{swp}}$  (Sec. II C). As a result, in the balanced chirp-alternating scheme [Eq. (11)] the first  $2N$  pulses become more and more chirped, before a reversal of the process to rewind back the rate. High optical chirping rates affect the  $V'$  couplings [Eq. (4)]. In our experiments, the single-photon detuning  $\Delta_e = 2\pi \times 10$  GHz is much larger than  $\delta_{\text{swp}}$ , and we numerically confirm that the increasingly chirped waveforms do not significantly affect the Raman dynamics in the  $\tilde{U}_{\text{uddu}}^{(4N)}$  scheme up to  $N = 6$ . Nevertheless, to avoid systematic errors associated with the digital OAWG pulse shaping [36], the chirp-rate accumulation is interrupted in this work by separating  $\tilde{U}_{\text{uddu}}^{(4N)}$  into  $N$  sets of four-pulse sequences, as described above.

We note that in the delay-line-based SDK scheme, there are extra ‘‘prepulses’’ and ‘‘postpulses’’ that interact with the atomic sample alone without any counterpropagating pulse to help driving the Raman transition [e.g., the first and last pulses in Fig. 2(b)]. Although these extra pulses impact negligibly the atomic hyperfine population and momentum transfer in this work, they cause extra dynamic phases, which need to be precisely compensated for during future coherent matterwave controls. Similar to the frequency domain Stark-shift compensation [43], for the nanosecond SDKs here one can fire additional pulses with suitable single-photon detunings to trim the overall dynamic phase [Eq. (9)]. Within nanoseconds, cold atoms hardly move to change the local laser intensity. We therefore expect the dynamic phase compensation to function well in the time domain.

## B. Optimizing adiabatic SDK

We prepare  $N_A \sim 10^5$   $^{85}\text{Rb}$  atoms in a compressed optical dipole trap at a temperature of  $T \sim 200$   $\mu\text{K}$  [36]. The atomic sample is optically pumped into the  $F = 2$ ,  $|b_m\rangle$  hyperfine states, elongated along  $z$ , with a characteristic radius of  $\sigma \approx 7$   $\mu\text{m}$  in the  $x$ - $y$  plane [Fig. 3(a)]. Immediately after the atoms released from the trap, multiple

SDKs programmed on the optical delay line with alternating  $\pm\mathbf{k}_R$ ,  $\mathbf{k}_R = 2k_0\mathbf{e}_z$  are applied to transfer photon momentum by repetitively inverting the atomic population between  $F = 2$ ,  $|b_m\rangle$  and the  $F = 3$ ,  $|a_m\rangle$  hyperfine states. Here  $k_0 = 2\pi/\lambda$  is the wave number of the D1 line SDK pulses at  $\lambda = 795$  nm.

We use a double-imaging technique to characterize the performance of the adiabatic SDKs, by simultaneously measuring the spin-dependent momentum transfer and population inversion (Appendix D). Specifically, immediately after the last of  $n$  SDK pulses, a probe pulse resonant to the D2 line  $F = 3 - F' = 4$  hyperfine transition is applied for  $\tau_p = 20$   $\mu\text{s}$  to record the spatial distribution of atoms in state  $|a\rangle$ , in the  $x$ - $z$  plane, with calibrated absorption imaging [15]. For atoms in  $|b\rangle$ , this probe is far detuned and weak enough not to perturb the motion. Next, after a  $\tau_{\text{TOF}} = 160$   $\mu\text{s}$  free-flight time, the second  $\tau_p = 20$   $\mu\text{s}$  probe pulse is applied to image all the atoms. For this purpose, during the time of flight an additional 50  $\mu\text{s}$  pulse along  $\mathbf{e}_x$ , resonant to  $F = 2 - F' = 3$  transition, repumps the  $|b\rangle$  atoms to  $|a\rangle$  for the second imaging. By comparing atom number  $N_a$  in state  $|a\rangle$  and the total atom number  $N_A = N_a + N_b$ , inferred from the first and second images, respectively, the probability of atoms ending up in  $|a\rangle$  can be measured as a function of the number of SDKs  $n$  as  $\rho_{aa,n} = N_a/(N_a + N_b)$ . In addition, by fitting both images to locate the center-of-mass vertical positions  $z_{1,2}$ , the atomic velocity  $v_n = \delta z/t_{\text{TOF}}$  can be retrieved to estimate the photon momentum transfer  $p_n = Mv_n$  in units of  $\hbar k_{\text{eff}}$ .

Typical  $v_n$  measurement results are given in Fig. 3(b). Here, for atoms prepared in  $|b\rangle$  states subjected to an  $n = 25$  SDK sequence starting with  $\tilde{U}_u(\mathbf{k}_R)\tilde{U}_u(-\mathbf{k}_R)$  (a  $2N = 24$  double SDK followed by an additional kick to drive the final Raman transition), the atomic population is largely in  $|a\rangle$  while  $v_n$  is unidirectional along  $\mathbf{e}_z$ . We optimize  $v_n$  by varying the peak Raman coupling amplitude  $C_R^{(0)}$  and sweep frequency  $\delta_{\text{swp}}$  of the adiabatic SDK pulses at fixed  $\tau_c$ . As in Fig. 3(b), for a fixed peak Raman pulse area  $\mathcal{A}_R$ , we generally find  $\delta_{\text{swp}}$  to be optimized for efficient photon momentum transfer when it matches  $C_R^{(0)}$  [see the arrow markers in Fig. 3(b)]. However, unlike two-level transfer [57] where an increased pulse area always leads to improved adiabaticity and population inversion robustness, here we find the peak  $\mathcal{A}_R \approx 9\pi$  reaches optimal to ensure the resilience of adiabatic SDK against the up to 50% intensity variation in the setup. Larger  $\mathcal{A}_R$  is accompanied by slow decrease of  $v_n$ , due to increased probability of spontaneous emission. Here, for  $\tau_c = 60$  ns, we need to attenuate  $C_R^{(0)} \approx 2\pi \times 150$  MHz to keep the peak  $\mathcal{A}_R \approx 9\pi$ . By using the full  $C_R^{(0)} \approx 2\pi \times 200$  MHz available in this work, we are able to reduce  $\tau_c$  to 40 ns while maintaining nearly identical momentum transfer efficiency at  $\delta_{\text{swp}} = 2\pi \times 150$  MHz.

### C. Inference of $f_{\text{SDK}}$

With the optimal  $\delta_{\text{swp}} = 2\pi \times 150$  MHz and peak  $\mathcal{A}_R \approx 9\pi$  at  $\tau_c = 40$  ns, we now apply  $n = 1 - 25$  SDKs to characterize the momentum transfer  $p_n = Mv_n$  and normalized population  $\rho_{aa,n}$  as a function of kicking number  $n$ . Typical results are given in Fig. 4. Here the momentum change  $p_n$  along  $\mathbf{e}_z$  is again unidirectional along  $z$  as in Fig. 4(a). The direction is conveniently reversed by programming  $\tilde{U}_u(-\mathbf{k}_R)$  first in the  $\pm\mathbf{k}_R$  alternating sequence, resulting in acceleration of atoms along  $-\mathbf{e}_z$  instead as in Fig. 4(c). In contrast, the hyperfine population  $\rho_{aa,n}$  is suppressed and revived after an even and odd number of SDKs, respectively, as demonstrated in Figs. 4(c) and 4(d). In addition,

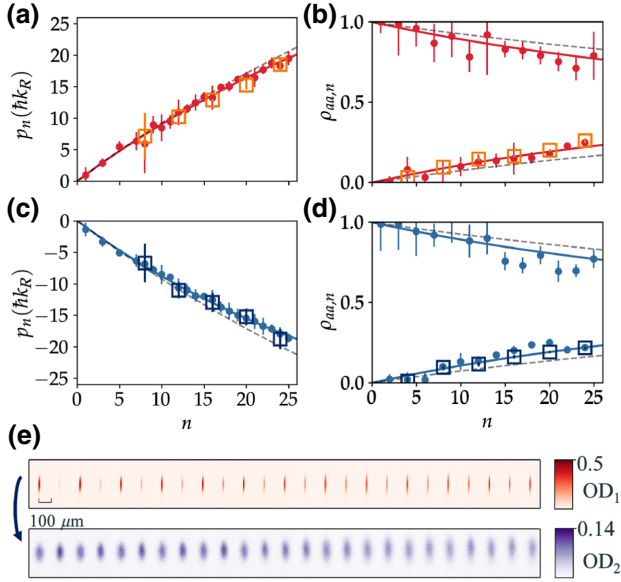


FIG. 4. Measurements of recoil momentum and hyperfine population transfer by multiple SDKs optimized at  $\tau_c = 40$  ns. Normalized momentum transfer  $p_n$  and hyperfine population  $\rho_{aa,n}$  versus kick number  $n$  are plotted in (a),(b)(c),(d), respectively. The atoms are initialized in  $F = 2$ ,  $|b_m\rangle$  states. Results for the  $\tilde{U}_{uu}^{(n)}(\pm\mathbf{k}_R)$  SDK sequence, starting with  $\tilde{U}_u(\mathbf{k}_R)\tilde{U}_u(-\mathbf{k}_R)$  and  $\tilde{U}_u(-\mathbf{k}_R)\tilde{U}_u(\mathbf{k}_R)$ , are plotted in top (a),(b) and bottom (c),(d) panels with disk symbols, respectively. Results for the balanced chirp-alternating  $\tilde{U}_{uddu}^{(4N)}(\pm\mathbf{k}_R)$  [Eq. (11)] with  $N = 2 - 6$  are plotted via open squares. For comparison, spontaneous-emission-limited  $p_n$  and  $\rho_{aa,n}$  according to numerical simulation are plotted with black dashed lines. A phenomenological fit (solid red and blue curves) suggests hyperfine Raman transfer efficiency  $f_R = 98.8(3)\%$  for the experimental data. See discussions in the main text for inference of  $f_{\text{SDK}} = 97.6(3)\%$  from the data. (e) Top: state-selective absorption images of atomic sample in  $F = 3$ ,  $\{|a_m\rangle\}$  states, probed immediately after  $n = 1 - 25$  SDK  $\tilde{U}_{uu}^{(n)}(\mathbf{k}_R)$  pulses. Bottom: corresponding absorption images of optically repumped atomic samples with  $\tau_{\text{TOF}} = 160 \mu\text{s}$ . Notice the  $n$ -odd measurements with higher  $\text{OD}_1$  suffer stronger probe-induced heating and thus wider  $\text{OD}_2$  distributions probed later, as expected.

we program a balanced chirp-alternating sequence  $n = 4N$  that combines  $\tilde{U}_u(\pm\mathbf{k}_R)$  with  $\tilde{U}_d(\mp\mathbf{k}_R)$  as  $\tilde{U}_{uddu}^{(4N)}(\pm\mathbf{k}_R)$  according to Eq. (11), a sequence, which will be detailed in Sec. IV for interferometric applications, with  $p_n$  and  $\rho_{aa,n}$  measurement results also given in Fig. 4 to demonstrate similar momentum and population transfer efficiency.

We estimate  $f_{\text{SDK}}$  by comparing the  $p_n$  and  $\rho_{aa,n}$  measurements as in Fig. 4 with precise numerical modeling detailed in Appendix B, taking into account the finite laser beam sizes and imperfect reflection with reflectivity  $r = |\kappa|^2$ . The comparison is facilitated by fitting both the measurement and simulating data according to a phenomenological model (Appendix C), which assumes that errors between successive SDKs are uncorrelated and are solely parametrized by  $f_R$ , a hyperfine Raman population transfer efficiency. The model predicts exponentially reduced increments  $|p_{n+1} - p_n|/\hbar k_{\text{eff}} = |\rho_{aa,n+1} - \rho_{aa,n}| = f_R(2f_R - 1)^n$  for  $f_R \approx 1$  by each SDK. From measurement data in Figs. 4(a)–4(d),  $f_R \approx 98.8\%$  can be estimated in both  $\tilde{U}_u(\mathbf{k}_R)$  and  $\tilde{U}_u(-\mathbf{k}_R)$  kicks [Figs. 4(a) and 4(c)], slightly less than spontaneous-emission-limited  $f_R \approx 99.2\%$  predicted by numerical simulation of the experiments, assuming perfect reflection with  $\kappa = 1$ .

We simply attribute the slightly reduced  $f_R$  from the theoretical value to imperfect retroreflection (Appendix E). In particular, we numerically find  $f_R$  reduces with  $f_{\text{SDK}}$  when  $\mathcal{E}_{1,2}$  are unbalanced in amplitudes, so that both spin leakage and spontaneous emission are increasingly likely to occur. Taking into account the independently measured  $r \approx 0.5$  in this work and with numerically matched  $f_R$ ,  $\varepsilon_{\text{leak}} \approx 2.5\%$  with  $\varepsilon_{\Delta m} \approx 0.5\%$  and  $\varepsilon_{\text{sp}} \approx 2\%$  can be estimated, respectively. We therefore infer from the combined analysis an  $f_{\text{SDK}} = 97.6(3)\%$  for the adiabatic SDK in this experiment, slightly less than the spontaneous-emission-limited  $f_{\text{SDK}} \approx 98\%$  for the nearly perfect adiabatic SDK. The numbers can be improved further by increasing  $\Delta_e$  to suppress spontaneous emission as well as the  $\Delta m$  leakage. It is important to note that while the imperfect reflection only moderately reduces  $f_{\text{SDK}}$ , the resulting imperfection of  $\mathbf{k}_R \leftrightarrow -\mathbf{k}_R$  swapping in successive  $\tilde{U}_u(\pm\mathbf{k}_R)$  control can greatly compromise the cancellation of dynamic phase  $\varphi_D$  in double SDK [Eq. (8)] [6,10], a topic to be detailed in Sec. IV D.

The adiabatic SDK demonstrated in this experimental section is the fastest realization to neutral atoms to date [6,10]. By equipping a more powerful laser, the SDK time can be reduced to a few nanoseconds or less [5]. A one-meter level compact delay line would then be able to resolve the counterpropagating pulses. Here, it is worth pointing out that the motion of the retroreflecting mirror [Fig. 2(a)] shifts the SDK diffraction phases [Eq. (5)] [34]. For interferometric measurements with long interrogation time (Sec. IV E), the end mirror for the compact delay line can be vibration-isolated as those in traditional atom interferometry [28–34].



#### IV. COHERENT CONTROL OF SPINOR MATTERWAVE

In the previous section, we experimentally characterize nanosecond adiabatic SDK by measuring the transfer of photon momentum and hyperfine population by a SDK sequence. A natural question to ask is whether it is possible to exploit the technique for coherent spinor matterwave control. As discussed in Sec. IID, for ideal SDKs the double SDK sequence [Eq. (8)] can be constructed to perform position-dependent phase gates. However, as to be illustrated in the following, the operation degrades rapidly with kick number  $N$  in the presence of coherent spin leakage among the  $2F_b + 1$   $\{|a_m\rangle, |b_m\rangle\}$  subspins (Sec. IV B), or when the nonperfect  $\mathbf{k}_R \leftrightarrow -\mathbf{k}_R$  swapping introduces additional dynamic phases (Sec. IV D).

Nevertheless, in this section we demonstrate that the  $\Delta m$  leakage and dynamic phases can be efficiently suppressed by the balanced chirp-alternating SDK sequence  $\tilde{U}_{uddu}^{(4N)}(\mathbf{k}_R)$  introduced in Sec. IIE [Eq. (11)] for faithful implementation of the  $U_K^{(4N)}(\mathbf{k}_R)$  phase gate by Eq. (8) to finely enable high-efficiency large momentum transfer [3]. We further numerically demonstrate the utility of the tailored adiabatic SDK sequence by simulating an area-enhanced atom interferometry sequence, using the experimental parameters both within and beyond this experimental work.

We notice control of spin leakage in quasi-two-level systems is an important topic in quantum control theory [64–66]. Previous studies on the topic typically involve a Morris-Shore transformation of the interaction matrix to decompose the multilevel dynamics [67]. However, as being schematically summarized in Fig. 1(b), the spin leakages are coherently driven through multiple paths with multiple Raman couplings to preclude a straightforward transformation, nor a direct application of the associated leakage-suppression techniques [64–66].

##### A. Average gate fidelity

To evaluate an imperfect double-SDK sequence  $\tilde{U}^{(2N)}(\mathbf{k}_R; \eta)$  as a quantum gate, we define an average fidelity for its performance on arbitrary spinor matterwave states of interest, e.g., spatially within the focal laser beam [Fig. 2(a)] and internally span the  $\{|a_m\rangle, |b_m\rangle\}$  subspace. The average fidelity is written as [52]

$$\mathcal{F}_m^{(2N)} = \left| \langle \psi_{m,j} | U_K^{(2N)\dagger}(\mathbf{k}_R) \tilde{U}^{(2N)}(\mathbf{k}_R; \eta) | \psi_{m,j} \rangle \right|_{\eta,j}^2. \quad (13)$$

Similar to Eq. (6), here  $\eta$  represents the Hamiltonian parameter in Eq. (4) including the atomic position  $\mathbf{r}$  of interest. For internal states the evaluation samples  $|\psi_{m,j}\rangle$  as the six eigenstates of  $\sigma_{x,y,z}^{(m)}$ , listing as  $\{|\psi_{m,j}\rangle\} = \{|b_m\rangle, |a_m\rangle, (|b_m\rangle \pm |a_m\rangle)/\sqrt{2}, (|b_m\rangle \pm i|a_m\rangle)/\sqrt{2}\}$ . With external motion ignored,  $\mathcal{F}_m^{(2N)} \approx 1$  ensures that the effectively instantaneous  $\tilde{U}^{(2N)}(\mathbf{k}_R; \eta)$

faithfully apply the phase gate to arbitrary spinor matterwave states near the beam focus, with certain laser intensity of interest.

For the convenience of related discussions, we define an average  $\Delta m$ -leakage probability, similar to Eq. (7), as

$$\varepsilon_{m,\Delta m}^{(n)} = 1 - \left\langle \langle \tilde{\psi}_{m,j}^{(n)} | \mathbf{1}^{(m)} | \tilde{\psi}_{m,j}^{(n)} \rangle \right\rangle_{\eta,j}, \quad (14)$$

where  $|\tilde{\psi}_{m,j}^{(n)}\rangle = \tilde{U}^{(n)}(\mathbf{k}_R; \eta) |\psi_{m,j}\rangle$  is defined as the final atomic state after the imperfect control. To exclude spontaneous emission, we simply renormalize to have  $\langle \tilde{\psi}_{m,j}^{(n)} | \tilde{\psi}_{m,j}^{(n)} \rangle = 1$  before the evaluation of the  $\Delta m$  leakage. Similar to Eq. (14), here the  $\Delta m$ -leakage probability is also evaluated for a specific  $m$  subspace of interest. Similar to Eqs. (6) and (7), here we expect  $\mathcal{F}_m^{(n)} \leq 1 - \varepsilon_{m,\Delta m}^{(n)}$ , i.e., any spin leakage results in gate infidelity.

##### B. Simple double SDK: spin leakage

We first consider the chirp-repeating double-SDK sequences  $\tilde{U}_{uu}^{(2N)}(\mathbf{k}_R)$  and  $\tilde{U}_{dd}^{(2N)}(\mathbf{k}_R)$  with Eq. (12). The simple sequences are widely applied in previous works to drive multiple recoil momentum transfer through both optical [57,68] and Raman excitations [6,10]. In the absence of the spin leakage, we expect both  $\tilde{U}_{uu}^{(2N)}(\mathbf{k}_R)$  and  $\tilde{U}_{dd}^{(2N)}(\mathbf{k}_R)$  to amplify the momentum transfer with cancelled dynamic phase [6,10], as suggested by Eq. (8).

Here, we numerically investigate the  $\Delta m$ -leakage probability  $\varepsilon_{m,\Delta m}^{(n)}$  and the gate fidelity  $\mathcal{F}_m^{(n)}$ , for an atom initialized in an  $\{|a_m\rangle, |b_m\rangle\}$  subspace being subjected to  $\tilde{U}_{uu}^{(n)}(\mathbf{k}_R)$ . With  $\Delta_e \gg \delta_{\text{swp}}$ , the results for  $\tilde{U}_{dd}^{(n)}(\mathbf{k}_R)$  are effectively identical. The Hamiltonian parameters in the simulation follow the experimental setup described in Sec. III for the  $^{85}\text{Rb}$  D1 line scheme (in particular,  $\delta_{\text{swp}} = 2\pi \times 150$  MHz), except here the reflective coefficient is set as  $\kappa = 1$  for simplicity, and  $\Gamma_e = 0$  to focus on the coherent control dynamics. To elucidate the role of laser intensity for the coherent control, we repeat the simulation while scanning the  $\mathbf{E}_{1,2}$  laser intensities in proportion, parametrized by the Raman pulse area  $\mathcal{A}_R$  in the following. Typical results for  $^{85}\text{Rb}$  are shown in the left panels of Figs. 5, 6, and 7.

We first discuss the  $\Delta m$ -leakage probability  $\varepsilon_{m,\Delta m}^{(n)}$  as a function of kick number  $n$  for typical  $\mathcal{A}_R = 9\pi$  presented in Fig. 5(a). Here, for  $n = 1$ , the tiny  $\varepsilon_{m,\Delta m}^{(n)}$  for all the  $m$  subspins are close to the single kick leakage of approximately 0.5% as being inferred experimentally. However, with increased  $n$ ,  $\varepsilon_{m,\Delta m}^{(n)}$  increases rapidly to approach unity for merely  $n \sim 20$ , i.e., atoms starting from any of the subspins  $\{|a_m\rangle, |b_m\rangle\}$  have a substantial probability of ending up in a different  $m$  subspace.

To investigate the laser intensity dependence, the  $\Delta m$  leakage  $\varepsilon_{m,\Delta m}^{(2N)}$  is further plotted in Figs. 6(a)–6(c) (left panels) as a function of both the kicking number  $n =$

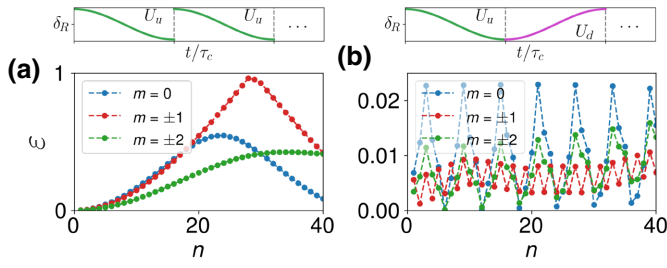


FIG. 5. Numerical results of spin leakage  $\varepsilon = \varepsilon_{m,\Delta m}^{(n)}$  for the traditional  $\tilde{U}_{uu}^{(n)}$  (left) and chirp-alternating  $\tilde{U}_{ud}^{(n)}$  (right) controls as a function of pulse number  $n$ . The peak Raman pulse area is  $\mathcal{A}_R = 9\pi$ . The corresponding two-photon detuning profiles are illustrated on top of (a),(b). Additional parameters for the simulations are according to the experimental Sec. III C.

$4N$  and the pulse area  $\mathcal{A}_R$ , for  $m = 0, \pm 1, \pm 2$  subspins, respectively. The choice of  $n = 4N$  is for comparison with the balanced chirp-alternating sequence to be discussed shortly. We see that over a broad range of pulse area  $\mathcal{A}_R$ , the spin-leakage probability  $\varepsilon_{m,\Delta m}^{(4N)}$  increases rapidly with  $4N$  in oscillatory fashions. There is hardly any continuous region of laser intensity with  $\varepsilon_{m,\Delta m}^{(4N)} < 0.1$ .

It is important to note that although the  $\Delta m$  leakages hardly affect the recoil momenta and hyperfine population transfers (Sec. III), they do limit the gate fidelity for faithful spinor matterwave control. The impact of spin leakage to average gate fidelity,  $\mathcal{F}_m^{(4N)}$ , is demonstrated by comparing Figs. 6(a)–6(c) with Figs. 7(a)–7(c). Here we

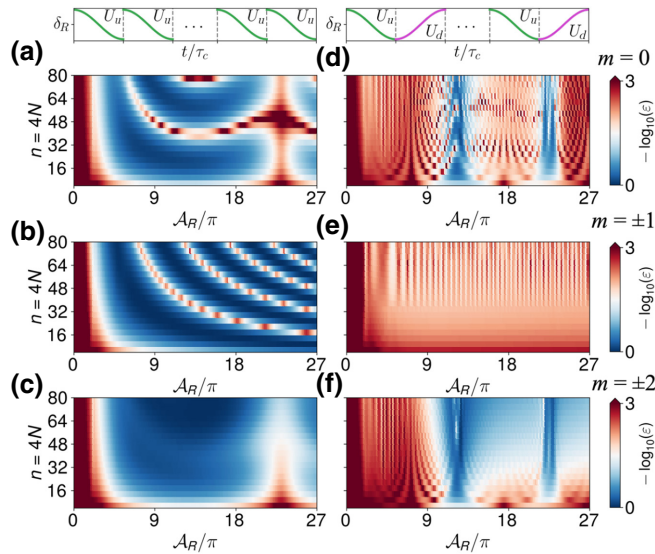


FIG. 6. Numerical results of spin leakage  $\varepsilon = \varepsilon_{m,\Delta m}^{(4N)}$  for the traditional  $\tilde{U}_{uu}^{(4N)}$  (left) and chirp-alternating  $\tilde{U}_{ud}^{(4N)}$  (right) as a function of kicking number  $4N$  and  $\mathcal{A}_R$ , with  $m = 0$  (a),(d),  $m = \pm 1$  (b),(e),  $m = \pm 2$  (c),(f). The two-photon detuning profiles are illustrated on top of (a),(d). Additional parameters for the simulations are according to the experimental Sec. III C.

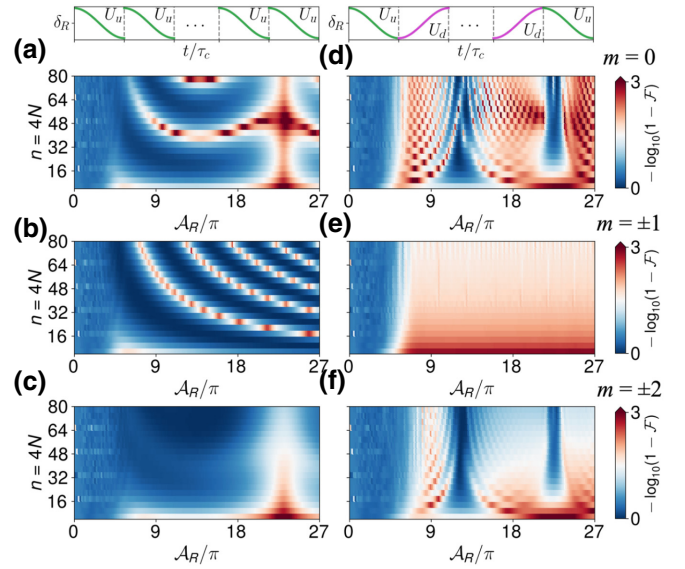


FIG. 7. Numerical results of gate infidelity  $1 - \mathcal{F}$  for the traditional  $\tilde{U}_{uu}^{(4N)}$  (left panels) and balanced chirp-alternating  $\tilde{U}_{uddu}^{(4N)}$  (right panels) controls. With  $\mathcal{F} = \mathcal{F}_m^{(4N)}$  and  $m = 0$  (a),(d),  $m = \pm 1$  (b),(e),  $m = \pm 2$  (c),(f). The two-photon detuning profiles are illustrated on top of (a),(d). Additional parameters for the simulations are according to Sec. III C.

see the gate infidelity  $1 - \mathcal{F}_m^{(4N)}$  closely follows  $\varepsilon_{m,\Delta m}^{(4N)}$  and hardly reach 0.1 over most laser intensities, except when the laser intensity is too low to adiabatically drive the Raman transition at all (with  $\mathcal{A}_R < 3\pi$  here) where we instead find  $\mathcal{F}_m^{(4N)} \approx 0.5$ , as expected.

Clearly, the coherent accumulation of  $\Delta m$ -leakage error as in Figs. 6(a)–6(c) needs to be suppressed before the adiabatic SDK sequence can be exploited for coherent control of spinor matterwave. Traditional methods for such suppression include applying a moderate quantization field to lift the Zeeman degeneracy [6,10,27,69]. This Zeeman-shift approach rules out the possibility of parallel multi-Zeeman spin-wave coherent control prescribed by Eq. (8). Furthermore, since the Zeeman shifts need to be substantially larger than the SDK bandwidth, a uniform field at a kilo-Gauss level is likely required for the nanosecond operations, which is not favored in precision metrology with alkaline atoms.

### C. Balanced chirp-alternating SDK scheme

We now demonstrate that the direction of chirps in an adiabatic sequence can be programmed to suppress the coherent accumulation of  $\Delta m$  leakage. Furthermore, by balancing  $\tilde{U}_{ud}^{(2N)}$  with  $\tilde{U}_{du}^{(2N)}$  as those in Eq. (11), the dynamic phase can be cancelled in  $\tilde{U}_{uddu}^{(2N)}$  to support faithful spinor matterwave phase gate. As to be clarified in the following, both the nonadiabatic spin-leakage suppression and dynamic phase cancellation are supported by time reversals of the driven spin dynamics, much like those

in the traditional spin-echo schemes, but is achieved here in the adiabatic SDK sequence to also ensure the laser intensity-error resilience. We note the benefit of alternating the chirp directions was also discovered in the context of two-level atom slowing with adiabatic pulses [40], but otherwise rarely explored before.

To understand why the accumulation of  $\Delta m$ -leakage error can be partly suppressed by the chirp-alternating  $\tilde{U}_{ud}^{(2N)}(\mathbf{k}_R)$  or  $\tilde{U}_{du}^{(2N)}(\mathbf{k}_R)$  sequence prescribed by Eq. (10), we come back to Eq. (4) to better understand the  $\Delta m = \pm 2$  leakage itself. In particular, for atom starting in  $|a_m\rangle$  or  $|b_m\rangle$  and subjected to a close-to-ideal adiabatic SDK control, with an  $H_u(\mathbf{r}, t)$  Hamiltonian during  $0 < t < \tau_c$  as prescribed in Sec. II E, the  $\Delta m = \pm 2$  transitions driven by  $V'$  are often a result of nonadiabatic couplings among subspins with nearly equal Stark shifts [for example, the  $m = \pm 1$  subspins in Fig. 1(b)]. By reversing the time dependence of the Hamiltonian, here with  $H_d(\mathbf{r}, t) = H_u(\mathbf{r}, \tau_d - t)$  within  $\tau_d < t < \tau_d + \tau_c$ , the sign of the nonadiabatic couplings are reversed. Such a sign reversal would lead to complete cancellation of the nonadiabatic transitions if the adiabatic states involved in the couplings are truly degenerate. Here, for atoms being addressed by the cross-linear polarized light, the fact that the  $m$  subspins are nearly degenerate makes the sign reversal efficient for the suppression of the unwanted leakages.

The simple picture of coherent leakage suppression is verified with numerical simulation in Fig. 5(b) for the chirp-alternating  $\tilde{U}_{ud}^{(2N)}(\mathbf{k}_R)$  sequence. Here, in contrast to the  $\tilde{U}_{uu}^{(2N)}(\mathbf{k}_R)$  case in Fig. 5(a), the spin leakage  $\varepsilon_{m,\Delta m}^{(n)}$  for all the  $m = 0, 1, 2$  oscillates and is overall efficiently suppressed. Comparing with  $m = \pm 1$  where the leakage is suppressed for even  $n$ , the leakage suppression from the  $m = 0, \pm 2$  subspin follows a more complicated pattern with an approximate periodicity of 4 to 5, suggesting more complex multilevel dynamics. We further investigate the leakage dynamics by plotting  $\varepsilon_{m,\Delta m}^{(n)}$  in 2D versus  $n$  and pulse area  $\mathcal{A}_R$ . The results for  $n = 4N$  are presented in Figs. 6(d)–6(f) to be compared with those in Figs. 6(a)–6(c). For the  $m = \pm 1$  subspins, the  $\Delta m$  leakage is suppressed to approximately 1%, limited by their residual couplings to the  $|a_m\rangle$  states with  $m = \pm 3$  [Fig. 1(a)]. In Appendix F we demonstrate that the spin-leakage suppression becomes perfect in species with nuclear spin  $I = 1.5$  ( $^{87}\text{Rb}$ -like) for the pair of  $m = \pm 1$  subspins. On the other hand, for  $m = 0, \pm 2$  subspins here, there are stripes of  $\mathcal{A}_R$  region (around  $\mathcal{A}_R = 12\pi$  and  $\mathcal{A}_R = 22\pi$  here, for example) where the leakage still accumulate with increased  $n = 4N$ , even though the suppression still works fairly well ( $\varepsilon_{m,\Delta m}^{(4N)} < 10\%$ ) for most of other  $\mathcal{A}_R$ . The intricate  $\mathcal{A}_R$ -dependent  $\varepsilon_{m,\Delta m}^{(2N)}$  as in Figs. 6(d) and 6(f) suggests that the difference of dynamic phases among  $m = 0, \pm 2$  subspins by each SDK is large enough to affect the coherent leakage cancellation [69].

We leave a detailed investigation of the intricate coupling dynamics for future work. Here, to construct faithful spinor matterwave control, we simply combine the  $\tilde{U}_{ud}^{(2N)}$  and  $\tilde{U}_{du}^{(2N)}$  sequence in Eq. (11) to form the balanced chirp-alternating SDK sequence. The idea is to exploit the time-reversal dynamics again to let the dynamic phases by the leakage-suppressing  $\tilde{U}_{du}^{(2N)}(\mathbf{k}_R)$  and  $\tilde{U}_{ud}^{(2N)}(\mathbf{k}_R)$  cancel each other.

We evaluate the average gate fidelity for realizing the quantum gate for  $U_K^{(4N)}(\mathbf{k}_R)$  [Eq. (8)] with  $\tilde{U}_{uddu}^{(4N)}(\mathbf{k}_R)$ . The results of  $\mathcal{F}_m^{(4N)}$ , with otherwise identical Hamiltonian parameters as those in Figs. 7(a)–7(c), are shown in Figs. 7(d)–7(f). Similar to Figs. 7(a)–7(c), here the infidelity  $1 - \mathcal{F}_m^{(4N)}$  for the  $\tilde{U}_{uddu}^{(4N)}(\mathbf{k}_R)$  sequence largely follows  $\varepsilon_{m,\Delta m}^{(4N)}$  for  $\tilde{U}_{ud}^{(4N)}$ . Therefore, the improvement is most significant for the  $m = \pm 1$  subspins to approach  $\mathcal{F}_m^{(4N)} \approx 98\%$  at  $4N = 80$ . For  $m = 0, \pm 2$  subspins, we also see improved gate fidelity  $\mathcal{F}_m^{(4N)} > 90\%$  span a substantial range of intensity for  $4N$  up to 80, with lower  $\mathcal{F}$  values for  $\mathcal{A}_R > 6\pi$  confined around specific  $\mathcal{A}_R$  only (deep-blue area). By moderately increasing  $\Delta_e$ , in Appendix F we demonstrate  $\mathcal{F} > 99\%$  with more confined low- $\mathcal{F}$  region after many kicks. Experimentally, the narrow low- $\mathcal{F}$  intensity region should be avoided for faithful multi-Zeeman spinor matterwave control of  $^{85}\text{Rb}$  with the balanced chirp-alternating scheme.

Finally, it is interesting to note that for the nearly perfect SDK, the gate infidelity  $1 - \mathcal{F}_m^{(4N)}$  is dominantly due to the spin leakage, as demonstrated by the remarkably similar  $1 - \mathcal{F}_m^{(4N)}$  and  $\varepsilon_{m,\Delta m}^{(4N)}$  data in Figs. 6 and 7. This is a result of dynamic phase cancellation in the adiabatic limit for both the  $\tilde{U}_{uu}^{(4N)}$  and  $\tilde{U}_{uddu}^{(4N)}$  sequences, when the  $\pm \mathbf{k}_R$  swapping as detailed next is perfect.

#### D. Robust cancellation of dynamic phase

The numerical results in Fig. 7 demonstrate that precise dynamic phase cancellation can be achieved by pairing  $\tilde{U}_{ud}^{(2N)}(\mathbf{k}_R)$  with  $\tilde{U}_{du}^{(2N)}(\mathbf{k}_R)$  into the balanced  $\tilde{U}_{uddu}^{(4N)}(\mathbf{k}_R)$ . In fact, we find that the dynamic phase cancellation in the balanced chirp-alternating scheme is substantially more robust than the traditional double-SDK by Eq. (8), as follows.

As in Sec. II D, the traditional method of dynamic phase cancellation [6] requires perfect  $\mathbf{k}_R \leftrightarrow -\mathbf{k}_R$  swapping for the successive  $U_K(\mathbf{k}_R)$   $U_K(-\mathbf{k}_R)$  controls. Practically the  $\mathbf{k}$ -vector swapping is typically accompanied by a modification of  $\mathbf{E}_{1,2}$  intensity ratio. For example, in the retroreflection setup [Fig. 2(a)], the amplitude of the reflected beam is reduced by a  $\kappa < 1$  factor due to the imperfect reflection, leading to unbalanced dynamic phases  $\varphi_D$  associated with  $\tilde{U}(\pm \mathbf{k}_R)$  to compromise their cancellation in the traditional double SDK [Eq. (8)] [6,10]. In fact, this systematic exists quite generally in retroreflection setups since the

two-photon shift  $\delta_0$  is sensitive to the laser intensities' ratios [25,61].

In contrast, here we notice that in the  $\tilde{U}_{uddu}^{(4N)}(\mathbf{k}_R)$  sequence [Eq. (11)] the dynamic phase by any  $\tilde{U}_{du}^{(2)}(\mathbf{k}_R)$  pair is expected to be cancelled by a  $\tilde{U}_{ud}^{(2)}(\mathbf{k}_R)$  pair later. In the adiabatic limit the cancellation is guaranteed, since for free atom starting from any specific two-level spin state, the sign of the chirp frequency  $\delta_{\text{swp}}$  dictates the adiabatic quantum number [60] and thus the sign of the dynamic phase in the adiabatic limit.

To demonstrate the robust dynamic phase cancellation, in Fig. 8, we compare  $\varphi_D$  according to Eq. (9) for the  $\tilde{U}_{uu}^{(4)}(\mathbf{k}_R)$  and  $\tilde{U}_{uddu}^{(4)}(\mathbf{k}_R)$  controls. The  $f_{\text{SDK}}$  values are given in the same plots, with which we see that the high  $f_{\text{SDK}}$  in the quasia-diabatic regime to be hardly affected even by a poor reflectivity  $r = |\kappa|^2 = 0.5$ . On the other hand, in contrast to Figs. 8(a)–8(c) (left) where  $r \approx 1$  is required for precise suppression of  $\varphi_D$  (blue line), in Figs. 8(d)–8(f) (right) the  $\varphi_D$  is largely suppressed so long as  $f_{\text{SDK}} \approx 1$ . It is worth noting that the residual variation of  $\varphi_{D,m}^{(4)}$  for  $\tilde{U}_{uddu}^{(4)}(\mathbf{k}_R)$  in Figs. 8(d)–8(f) in the quasia-diabatic regime are coupled to the coherent spin-leakage dynamics [Figs. 6(d)–6(f)]. Nevertheless, even for  $r = 0.5$  similar to the experimental situation in this work, the residual phase variations are still limited to  $|\varphi_{D,m}^{(4)}| < 50$  mrad for the  $m = 0, \pm 2$  subspins, and  $|\varphi_{D,m}^{(4)}| < 3$  mrad for the  $m = \pm 1$  subspins, respectively.

### E. Area-enhancing atom interferometry

So far in this section, we have shown that matter-wave phase gate prescribed by the ideal double SDK [Eq. (8)] can be faithfully implemented by the balanced chirp-alternating sequence  $\tilde{U}_{uddu}^{(4N)}(\mathbf{k}_R)$ , to coherently shift any  $|a_m\rangle, |b_m\rangle$  components of hyperfine spinor matterwave with opposite  $\pm 4N\hbar\mathbf{k}_R$  momentum within nanoseconds. For control parameters in this experimental demonstration, our numerical results already suggest fairly high gate fidelity with efficient suppression of the coherent spin leakage and inhomogeneous dynamic phase. In future work, by increasing  $\Delta_e/\Gamma$  and  $\Delta_e/\Delta_{\text{HFS},e}$  ratios and the laser intensities  $I_{1,2}$  in proportion (Appendix F), the residual imperfections can be further suppressed to meet the exquisite requirements in the applications of quantum information processing [11,12,16,17] and quantum enhanced atom interferometry [18–21].

Here, to demonstrate the utility of the adiabatic SDK sequence for precision measurements, we numerically investigate a simple atom interferometry scheme [3,6,10] where an “enclosed area”  $A$  is enhanced by the  $\tilde{U}_{uddu}^{(4N)}(\pm\mathbf{k}_R)$  sequences. As in the Mach-Zehnder configuration in Fig. 9(a), we consider the two spinor matterwave components forming a loop to interfere at  $t = 2T$  (the dashed lines). When sensing a constant force field, the

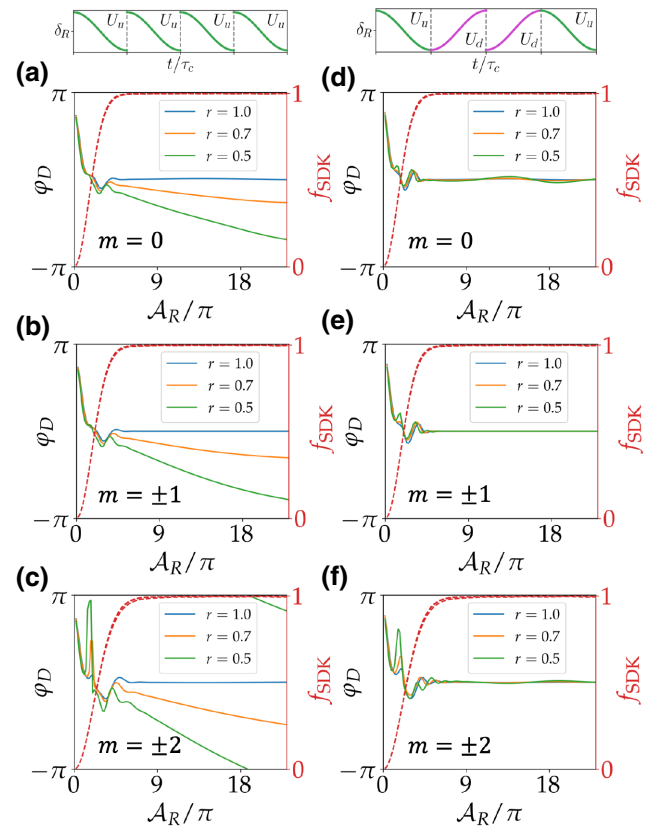


FIG. 8. Unbalanced dynamic phase  $\varphi_D = \varphi_{D,m}^{(4)}$  according to Eq. (9) versus pulse area  $\mathcal{A}_R$  for  $m = 0$  (a),(d),  $m = \pm 1$  (b),(e) and  $m = \pm 2$  (c),(f) subjected to  $\tilde{U}_{uu}^{(4)}(\mathbf{k}_R)$  (left) and  $\tilde{U}_{uddu}^{(4)}(\mathbf{k}_R)$  (right) controls. The corresponding two-photon detuning profiles are illustrated on top of (a),(d). Parameters for the simulations are according to the experimental Sec. III C, except here the mirror reflectivity  $r$  varies. The red dashed lines give  $f_{\text{SDK}}$  for single kicks (different  $r$  curves closely overlap).

difference of matterwave phase shifts along the two paths,  $\Delta\Phi \propto A$  associated with the path-dependent diffraction phase [43], is read out interferometrically [44,70]. Here  $A$  is the spatial-temporal “area” enclosed by the loop. When the duration of the pulsed rotations are negligibly short relative to the “interrogation time”  $T$ , then  $A = v_R T^2$  is easily evaluated. Here  $v_R = \hbar k_{\text{eff}}/M$  is the photon recoil velocity. Clearly, when the atomic interferometer acts as a force sensor, its sensitivity increases with  $A$ . In fact, to achieve as large “area”  $A$  as possible within a measurement time  $T$  is of general importance to precision measurements with light pulse atom interferometry [3,34,44].

More specifically, the enclosed area is defined as  $A = \int_0^{2T} \Delta z(t) dt$  during a three-pulse Raman interferometry sequence by integrating the relative displacement  $\Delta z(t)$  between the two matterwave diffraction paths under the three operations as splitter ( $t = 0$ ), mirror ( $t = T$ ), and combiner ( $t = 2T$ ). We generally refer the idealized local spin rotations as  $R_\varphi(\theta) = \cos(\theta/2)\mathbf{1}$

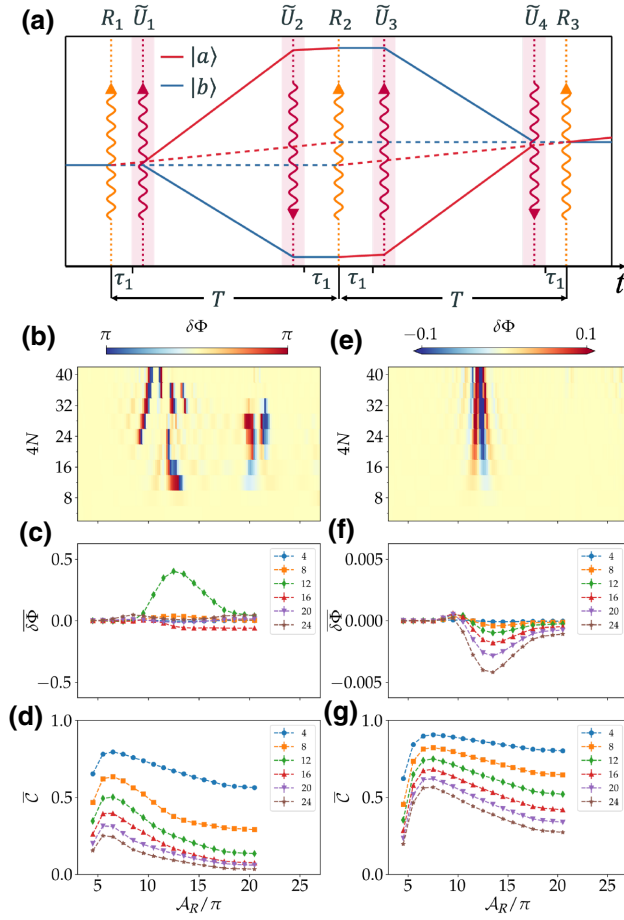


FIG. 9. Enhancing the enclosed area of an atom interferometer with four  $\tilde{U}_{uddu}(\pm\mathbf{k}_R)$  SDK sequences. (a) Schematic of the interferometry scheme. The dashed lines at  $t = 0, T, 2T$  represent regular Raman interferometry controls for the  $R_1 = R_\varphi(\pi/2)$  splitter,  $R_2 = R_\varphi(\pi)$  mirror and  $R_3 = R_\varphi(\pi/2)$  combiner of the spinor matterwave, respectively, with  $\varphi = \mathbf{k}_R \cdot \mathbf{r}$ . The atomic wave functions in  $|b\rangle$  and  $|a\rangle$  states are represented by the blue and red lines [3]. The four thick vertical lines at  $t = \tau_1, T - \tau_1, T + \tau_1, 2T - \tau_1$  with red curved arrows represent  $\tilde{U}_1 = \tilde{U}_{uddu}^{(4N)}(\mathbf{k}_R)$ ,  $\tilde{U}_2 = \tilde{U}_{uddu}^{(4N)}(-\mathbf{k}_R)$ ,  $\tilde{U}_3 = \tilde{U}_{uddu}^{(4N)}(-\mathbf{k}_R)$ , and  $\tilde{U}_4 = \tilde{U}_{uddu}^{(4N)}(\mathbf{k}_R)$  sequences, respectively. We consider  $\tau_1 \ll T$ . By properly choosing the  $\tau_1/T$  ratio, spurious interference by multiple imperfect controls can be suppressed, and are not included in the simulations. (b)–(d) The interferometry phase offset  $\delta\Phi$  and contrast  $\mathcal{C}$  as a function of SDK number  $n = 4N$  and pulse area  $\mathcal{A}_R$ . Here the single-photon detuning is chosen as  $\Delta_e = -3.3 \omega_{\text{HFS},g}$ . The simulations average over  $m = -2, -1, 0, 1, 2$  states, and include  $\Gamma_e = 0.017 \omega_{\text{HFS},e}$  as for the case of  $^{85}\text{Rb}$ . The phase offsets and interferometry contrasts for the simulated signals locally averaged over a 50% intensity distribution are given in (c),(d). The data in (e)–(g) are similar to (b)–(d), but with an increased single-photon detuning of  $\Delta_e = -6.6 \omega_{\text{HFS},g}$ .

$+ i \sin(\theta/2)(e^{i\varphi}\sigma_+ + e^{-i\varphi}\sigma_-)$  for the Raman interferometer, for any spin state within  $\{|a_m\rangle, |b_m\rangle\}$ . Here  $\varphi = \mathbf{k}_R \cdot \mathbf{r}$  is the local Raman optical phase. Notice the

spatial-dependent  $R_\varphi(\theta)$  rotation can, in principle, be generated by the Eq. (4) Hamiltonian [71] as phase-coherent “half” and “full” kicks. The splitter and mirror operations in the standard light Raman interferometer can then be expressed as  $R_1 = R_\varphi(\pi/2)$ ,  $R_2 = R_\varphi(\pi)$  and  $R_3 = R_\varphi(\pi/2)$ , respectively, to manipulate the spin states while imparting the  $\pm\hbar\mathbf{k}_R$  photon recoil momentum.

We now consider enhancing the enclosed area  $A$  of the standard three-pulse Raman interferometer with the chirp-alternating SDK sequence. In particular, we consider the Fig. 9(a) scheme with the spinor matterwave diffraction paths marked with solid lines: a  $\tilde{U}_1 = \tilde{U}_{uddu}^{(4N)}(\mathbf{k}_R)$  is first applied at  $t = \tau_1$  to increase the momentum displacement between the two interfering paths from  $\Delta\mathbf{p} = \hbar\mathbf{k}_R$  by  $R_\varphi(\pi/2)$  to  $\Delta\mathbf{p} = (2 \times 4N + 1)\hbar\mathbf{k}_R$  with the spin-dependent kicks. This  $\Delta\mathbf{p}$  enhancement is followed by an opposite  $\tilde{U}_2 = \tilde{U}_{uddu}^{(4N)}(-\mathbf{k}_R)$  at  $t = T - \tau_1$  before the  $R_2$  operation to recover the initial  $\Delta\mathbf{p}$ . To ensure that the interfering paths spatially overlap at  $t = 2T$ , an additional pair of opposite momentum boosts,  $\tilde{U}_{3,4}$  are applied at  $t = T + \tau_1$  after the  $R_2$  and  $t = 2T - \tau_1$  before the  $R_3$  operation, respectively. By properly choosing the  $\tau_1/T$  ratio, spurious interference by imperfect  $R_{1,2,3}$  and  $\tilde{U}_{1,2,3,4}$  controls can be suppressed [72,73]. With  $T \gg \tau_1$ , the enclosed area of the resulting interfering loop is enhanced to  $A' = (2 \times 4N + 1)A$ .

For the numerical simulation, we consider at  $t = 0$  the atomic state to be initialized at certain  $|b_m\rangle$  and subjected to the  $\tilde{U}_{uddu}^{(4N)}(\mathbf{k}_R)$ -enhanced three-pulse interferometry sequence. The output atomic state, right before the final matterwave combiner  $R_3$ , can then be written as  $|\psi_m(\mathbf{r}, 2T^-)\rangle = U_{\text{AI}}|c_m\rangle$ , with  $U_{\text{AI}} = U_f(\tau_1)\tilde{U}_4 U_f(T - 2\tau_1)\tilde{U}_3 R'_2 \tilde{U}_2 U_f(T - 2\tau_1)\tilde{U}_1 R'_1$  to be  $\mathbf{r}$  dependent. Here  $U_f(t)$  designates free propagation of matterwave for time  $t$ . The  $R'_1 = U_f(\tau_1)R_1$ ,  $R'_2 = U_f(\tau_1)R_2 U_f(\tau_1)$  takes into account the free propagation of matterwave between the standard  $R_j$  and area-enhancing  $\tilde{U}_j$  sequences. We numerically evaluate  $|\psi_m(z, 2T^-)\rangle$  for 1D spinor matterwave between  $0 < z < \lambda/2$  ( $\lambda$  is the optical wavelength), as described in Appendix B. To focus on the performance of SDK, we set  $R_{1,3}$  as perfect  $\pi/2$  pulses and  $R_2$  as perfect  $\pi$  mirror pulse, respectively. A further simplification sets  $\mathbf{k}_R = 0$  for the idealized  $R_{1,2,3}$  controls, with which we numerically evaluate  $\langle \Sigma_j \rangle = \langle \psi_m(z, 2T^-) | \Sigma_j | \psi_m(z, 2T^-) \rangle_{z,m}$  for an initially unpolarized atomic sample. Here  $\Sigma_j = \sum_{m'=-F_b}^{F_b} \sigma_j^{(m')}$  are summed over all  $m$  subspins for Pauli matrices with  $j = x, y, z$ .  $\Sigma_j$  corresponds to observables of experimental measurements in which Zeeman sublevels are not resolved, as in most atom interferometry experiments with hyperfine state-dependent fluorescence readouts [34].

With  $U_f$  chosen as free 1D propagation, the values of  $\tau_1$  and  $T$  affect only contributions of spurious interfering paths into the final readouts [72,73] in the simulation. With

$R_{1,2,3}$  set as ideal, the spurious interfering paths are from imperfect  $\tilde{U}_{1,2,3,4}$  diffractions only. Notably, since successive adiabatic SDKs here within each  $\tilde{U}_j$  last merely tens of nanoseconds, the spatial displacements among the spurious interfering paths are negligibly small comparing with the typical coherence length of cold-atom samples, and therefore do not alter the matterwave dynamics [74,75]. We randomly sample the atomic initial position and velocity to numerically verify that the residual spurious interference are indeed suppressible. Practically, to generate the results in Figs. 9(b)–9(d) with all spurious interference removed in an efficient manner, we simply apply a digital filter to remove unwanted diffraction orders after each  $\tilde{U}_j$  sequence.

We are particularly interested in the interferometry contrast  $\mathcal{C}$  and diffraction phase offset  $\delta\Phi$ . The contrast  $\mathcal{C}$  sets the quality of the final matterwave interference fringes. The phase offset  $\delta\Phi$ , stemming from the unbalanced dynamic phase by the four  $\tilde{U}_{uddu}$  sequences, enters the interferometry readout as systematic bias against any precision measurements or controls. We evaluate the interferometry contrast as  $\mathcal{C} = \sqrt{\langle \Sigma_x \rangle^2 + \langle \Sigma_y \rangle^2}$ , keeping in mind the ideal  $R_3$  rotates  $\Sigma = \{\Sigma_j\}$  by  $90^\circ$  for the final population readouts. The diffraction phase offset is instead evaluated as  $\delta\Phi = \arg[\langle \Sigma_x \rangle + i\langle \Sigma_y \rangle] - \Phi_0$  with  $\Phi_0$  to be the relative phase between  $|a_m\rangle$  and  $|b_m\rangle$  right after the ideal  $R_1$  splitter. Typical numerical results are presented in Figs. 9(b)–9(d). The simulation is again performed on the  $^{85}\text{Rb}$  D1 line, here with spontaneous emission included. For Figs. 9(b)–9(d) on the left panel, the control laser parameters are chosen close to this experimental work, with  $\Delta_e = -3.3 \omega_{\text{HFS},g}$  so both  $\varepsilon_{\text{sp}}$  and  $\varepsilon_{\Delta m}$  are quite substantial. Nevertheless, we find four  $n = 4N = 12$  chirp-alternating SDKs can be applied for a 25-fold enhancement of interferometry enclosed area, at a moderate expense of reduced contrast to  $\mathcal{C} \approx 0.5$  (which is still highly useful [34]), with  $\delta\Phi < 0.01$  to be experimentally calibrated when necessary. Here, to avoid excessive spontaneous emission and coherent leakage [Figs. 6(d)–6(f)], the peak  $\mathcal{A}_R \approx 6 - 8\pi$  needs to be chosen [Figs. 9(b)–9(d)]. On the other hand, by doubling the single-photon detuning to  $\Delta_e = -6.6 \omega_{\text{HFS},g}$  (with laser intensity increased in proportion to maintain the Raman Rabi frequency),  $\varepsilon_{\text{sp}}$  are halved, while the impact of  $\varepsilon_{\Delta m}$  leakage are dramatically suppressed in the  $\tilde{U}_{uddu}$  sequence [Figs. 9(e)–9(g), also see Appendix F] [76]. The further detuned  $\tilde{U}_{uddu}$  sequence should thus support up to 50-fold enhancement of interferometry enclosed area, with spontaneous-emission-limited  $\mathcal{C} > 0.5$  contrast.

## V. DISCUSSIONS

Significant aspects of advanced quantum technology today are based on controlling alkaline atoms through their center-of-mass motion and ground-state hyperfine

interaction. The two long-lived degrees of freedom can be entangled optically by transferring photon recoil momentum with Raman excitations. The tiny atomic recoil effect can be amplified by the repetitive application of such excitations. The spin-dependent large momentum transfer is expected to improve the scalability for precision measurements in atom interferometry [3,6,10] and for quantum information processing with trapped ions [5,11–13,17]. Practically, unlike interrogating microscopically confined single ions where Raman excitation with multiple-THz single-photon detuning is feasible [8,39], addressing larger samples prefers efficient excitations at moderate single-photon detunings. The seemingly unavoidable imperfections associated with spin leakages and dynamic phases need to be managed in nontraditional ways, for achieving the high-speed, high-fidelity control with intensity-error resilience required by the next-generation quantum technology [16–21].

In this work, we have demonstrated a novel configuration of adiabatic SDK implemented on an optical delay line, which is able to reach the speed limit of Raman SDK control [5,39], featuring robust intensity-error resilience, while maintaining various advantages of optical retroreflection established for precision atom interferometry. The experimental characterization of the technique is limited to the hyperfine population and spin-dependent momentum transfers, but we clarify in Sec. IV that high-precision phase gates enabling spin-dependent large momentum transfer can be efficiently realized at the moderate single-photon detuning, by properly programming the chirp direction to suppress the accumulation of coherent errors. We have provided numerical evidence that the chirp-balanced SDK scheme support faithful, parallel  $\Delta m = 0$  control of multi-Zeeman spinor matterwave, with giant spin-dependent forces applied within nanoseconds to rapidly shift the phase-space spin separation, even with the approximately 10-mW laser power as in this work. Since within nanoseconds various low-frequency noises including those due to matterwave dispersion are negligible for cold atoms, we expect accurate implementation of the full scheme to be benchmarked in future interferometric measurements.

Our work suggests that Raman SDK can be dynamically perfected against multilevel couplings and dynamic phase broadening, for error-resilient parallel control of multiple hyperfine spinors within nanoseconds, with exquisite precision. Operating in the unconventional regime of Raman control [25,41], the technique requires relatively moderate laser intensity when comparing with similar techniques for controlling microscopically confined ions [5,16,17]. Nevertheless, we note the high-speed SDK demonstrated in this work is realized by weakly focusing the milliwatt level output from OAWG [36] to a mesoscopic sample to reach the required intensity. Our technique is immediately useful for coherently controlling mesoscopic ultracold samples

for quantum simulation [77,78] and atom interferometry [79–82]. By improving the peak power of the nanosecond pulses [14,83–86], our method may drastically enhance the practical benefits of large-momentum beam splitting in Raman atom interferometry [3,6,10], and to support ultraprecise matterwave control for quantum enhanced technologies [18–21].

### ACKNOWLEDGMENTS

We thank Yudi Ma and Xing Huang for experimental assistance. We are grateful to Professor Yiqiu Ma for insightful comments on the paper, and to Professor Xiaopeng Li and Professor Haidong Yuan for helpful discussions. We acknowledge support from National Key Research Program of China under Grants No. 2016YFA0302000 and No. 2017YFA0304204, from NSFC under Grant No. 12074083.

### APPENDIX A: FULL HAMILTONIAN

The theoretical analysis as well as numerical simulation in this work is based on the full light-atom interaction Hamiltonian on the D1 line. Following the notation in the main text, the effective, non-Hermitian Hamiltonian is written as

$$H_{\text{eff}}(\mathbf{r}, t) = \hbar \sum_e (\omega_e - \omega_{e0} - i\Gamma_e/2) \sigma^{e|e|} + \hbar \sum_{c=a,b} (\omega_c - \omega_{g0}) \sigma^{c|c|} + \frac{\hbar}{2} \sum_{c=a,b} \sum_e \Omega_{c|e|}^j(\mathbf{r}, t) \sigma^{c|e|} + \text{h.c.} \quad (\text{A1})$$

Here  $\omega_{e0}, \omega_{g0}$  are decided by the energy of reference level in the excited- and ground-state manifolds, respectively, chosen as the top hyperfine levels in this work. The laser Rabi frequency,

$$\Omega_{e|a_m(b_n)}^j(\mathbf{r}, t) \equiv -\frac{\langle e| \mathbf{d} \cdot \mathbf{e}_j \mathcal{E}_j(\mathbf{r}, t) a_m(b_n) \rangle}{\hbar}, \quad (\text{A2})$$

is accordingly written in the  $\omega_{e0, g0}$  frame under the rotating-wave approximation.  $\mathbf{d}$  to be the atomic electric dipole operator. The  $\sigma^{a_m|e|} = |a_m\rangle \langle e|$ ,  $\sigma^{e|a_m} = |e\rangle \langle a_m|$  are the raising and lowering operators between states  $|a_m\rangle$  and  $|e\rangle$ . Similar  $\sigma$  operators are defined for all the other  $|a_m\rangle$ ,  $|b_n\rangle$ , and  $|e\rangle$  state combinations.

The full  $H_{\text{eff}}$  in Eq. (A) is rewritten as Eq. (4) in the main text. For weak off-resonant pulses and to facilitate understanding of ground-state Raman interaction, we can also adiabatically eliminate the excited states to approximately

have

$$H_{\text{eff}}(\mathbf{r}, t) \approx \hbar \sum_e \sum_{j=1,2} \frac{\Omega_{a_m|e|}^j \Omega_{a_n|e|}^{j*}}{4(\nu_j - \omega_{ea})} \sigma^{a_m|a_n} + \frac{\Omega_{b_m|e|}^j \Omega_{b_n|e|}^{j*}}{4(\nu_j - \omega_{eb})} \sigma^{b_m|b_n} + \hbar \sum_e \frac{\Omega_{a_m|e|}^1 \Omega_{b_n|e|}^{2*}}{4\Delta_e} e^{i\mathbf{k}_R \cdot \mathbf{r}} \sigma^{a_m|b_n} + \text{h.c.} + \hbar \sum_e \frac{\Omega_{a_m|e|}^2 \Omega_{b_n|e|}^{1*}}{4\Delta_e} e^{i\mathbf{k}_R \cdot \mathbf{r}} e^{i2\omega_{ab}t} \sigma^{b_n|a_m} + \text{h.c.}, \quad (\text{A3})$$

with the convention of summing over repeated  $m, n, l$  indices [50]. The single photon detuning is defined as  $\Delta_e = \omega_1 - \omega_{ea} = \omega_2 - \omega_{eb}$ . The vector  $\mathbf{k}_R = \mathbf{k}_2 - \mathbf{k}_1$  is the  $\mathbf{k}$  vector associated with the Raman transition driven by the counterpropagating pulses.

The Raman coupling associated with  $\sigma^{b_n|a_m}$  in line 2 of Eq. (A3) is accompanied by a  $\pm \hbar \mathbf{k}_R$  momentum transfer to the spinor matterwave. Similarly, the “counter-rotating” term in line 3 of Eq. (A3) leads to an opposite,  $\mp \hbar \mathbf{k}_R$  momentum transfer. For smooth laser pulses with bandwidth  $\delta\omega \ll \omega_{ab}$  to be discussed, this “counter-rotating” Raman process is energetically suppressed. The regime of resonant Raman interaction with directional momentum transfer is the focus of this work.

### APPENDIX B: NUMERICAL MODEL

We numerically simulate the evolution of 1D spinor matterwaves with full D1 light-atom interactions [63,87] driven by the counterpropagating Raman pulses as in Figs. 1 and 2. To account for radiation damping, we follow a stochastic wave-function method [88] to evaluate the wave function  $|\psi(\mathbf{r}, t)\rangle$  for atom at location  $\mathbf{r}$  under the non-Hermitian Hamiltonian  $H_{\text{eff}}$  [see Eq. (A) with non-Hermitian part  $\hbar \sum_e i\Gamma_e \sigma^{e|e|}/2$  in the first line]. Here  $\Gamma_e$  is the natural linewidth of the D1 line. The simulations treat both the internal and external motion of the spinor matterwave quantum mechanically. For the purpose, we sample  $|\psi(\mathbf{r}, t)\rangle$  densely over a uniform grid within  $0 < z < \lambda/2$  and sparsely in the  $x$ - $y$  plane, and follow a split-operator method to evaluate internal and external atomic motion numerically with interleaved steps. Taking advantage of the short  $\tau_c$  for single SDK, the internal state dynamics is evaluated within a single step with frozen external motion under a local  $|\psi(\mathbf{r})\rangle$  basis, with atomic position  $\mathbf{r}$  treated as a parameter of  $H_{\text{eff}}$ . The evaluation of observables later is normalized by  $\mathcal{N} = \sum_{\mathbf{r}} \langle \psi(\mathbf{r}, t=0) | \psi(\mathbf{r}, t=0) \rangle$ , with corrections from stochastic contributions to be discussed shortly. Between SDKs, a Fourier transform along  $\mathbf{e}_z$  can be performed to evolve the free-flying spinor

matterwave along  $z$  if necessary. To save computation resources, the relatively simple atomic dynamics in the  $x$ - $y$  plane is ignored. To evaluate momentum distribution of spinor matterwave, we simply perform a Fourier transform to the space-dependent  $\langle c_m | \psi(\mathbf{r}, t) \rangle$  for any specific spin state  $|c_m\rangle$ .

Beyond the coherent evolution, the simulation complexity is substantially reduced by skipping the evaluation of stochastic trajectories heralded by a single ‘‘quantum jump’’ [53,54]. Specifically, after each pulsed interaction, the trajectories suffering a quantum jump are simply assumed to repopulate  $\{|a\rangle, |b\rangle\}$  in a uniform manner with properly shifted photon recoil momentum. Without further evolution, these trajectories contribute to the evaluation of incoherent, single-time observables such as hyperfine population and photon momentum transfer. The overall probability of spontaneous emission is determined by the norm of the final wave function,  $\varepsilon_{\text{sp}} = 1 - 1/\mathcal{N} \sum_{\mathbf{r}} \langle \psi(\mathbf{r}, \tau_{\text{tot}}) | \psi(\mathbf{r}, \tau_{\text{tot}}) \rangle$ , after a total evolution time  $\tau_{\text{tot}}$ . The simplification is generally justified for evaluating coherent observables of interest, since the expectation values shifted stochastically lead to zero coherent contributions. For the incoherent observables such as average photon momentum and hyperfine population, the simplification is supported by the simple D1 structure under consideration here [63], where a single spontaneous emission effectively randomizes the following Raman interaction dynamics.

### APPENDIX C: A MARKOVIAN MODEL FOR $f_{\text{SDK}}$ ESTIMATION

For atoms subjected to multiple SDKs, the dynamics of spinor matterwave that deviates from the ideal control can be depicted as diffusing in a ‘‘momentum lattice’’ [15]. Our numerical simulation suggests that with fair efficiency of single adiabatic pulse to achieve hyperfine transfer efficiency of  $f_R > 95\%$ , the resulting average momentum  $p_n$  and population  $\rho_{aa/bb,n}$  roughly follow a simple Markovian model. The model assumes that both the momentum and population transfer by the next kick are decided by the present population difference  $\rho_{aa} - \rho_{bb}$  only. The details of the Markovian model are described as follows.

Suppose that after  $n$  kicks, the atomic ensemble is with momentum  $p_n$  (in unit of  $\hbar\mathbf{k}_R$ ) and population contrast  $\mathcal{C}_n \equiv |\rho_{aa,n} - \rho_{bb,n}|$ , then the next kick will impart momentum as

$$\Delta p_{n+1} = p_{n+1} - p_n = f_0(1 - \varepsilon_{\text{sp}}/2)\mathcal{C}_n, \quad (\text{C1})$$

where  $f_0$  is the hyperfine population transfer efficiency in the absence of the spontaneous emission. Here we assume that during the single pulse process, the spontaneous emission occurs with a uniform distribution of probability, thus the associated population recycled to the ground states acquires half of  $\hbar\mathbf{k}_R$  momentum on average.

Similarly, the population distribution can be written as

$$\begin{aligned} \rho_{aa,n+1} &= (1 - \varepsilon_{\text{sp}}) \left[ (1 - f_0) \frac{1 + \mathcal{C}_n}{2} + f_0 \frac{1 - \mathcal{C}_n}{2} \right] \\ &\quad + \varepsilon_{\text{sp}}/2, \\ \rho_{bb,n+1} &= (1 - \varepsilon_{\text{sp}}) \left[ f_0 \frac{1 + \mathcal{C}_n}{2} + (1 - f_0) \frac{1 - \mathcal{C}_n}{2} \right] \\ &\quad + \varepsilon_{\text{sp}}/2, \end{aligned} \quad (\text{C2})$$

so that

$$\mathcal{C}_{n+1} = (1 - \varepsilon_{\text{sp}})(2f_0 - 1)\mathcal{C}_n. \quad (\text{C3})$$

We define Raman transfer efficiency as  $f_R = f_0(1 - \varepsilon_{\text{sp}}/2)$ . When both  $f_0$  and  $1 - \varepsilon_{\text{sp}}$  are close to unity, Eqs. (C1)–(C3) can be approximated as

$$\begin{aligned} p_{n+1} - p_n &= f_R \mathcal{C}_n, \\ \mathcal{C}_{n+1} &= (2f_R - 1)\mathcal{C}_n. \end{aligned} \quad (\text{C4})$$

With the recursion relations by Eq. (C4), we arrive at

$$\begin{aligned} p_n &= f_R \frac{1 - (2f_R - 1)^n}{1 - (2f_R - 1)}, \\ \mathcal{C}_n &= (2f_R - 1)^n. \end{aligned} \quad (\text{C5})$$

Finally, we remark that for the Raman SDK, there is a slight difference of spontaneous emission loss for single kicks between the  $a \rightarrow b$  and  $b \rightarrow a$  process. As we consider repetitive SDK with  $n$  up to a quite large number (e.g.,  $n_{\text{max}} = 25$  in our experiment), we effectively set the same  $\varepsilon_{\text{sp}}$  parameter for the opposite population transfer processes.

### APPENDIX D: ABSORPTION IMAGING ANALYSIS

In Sec. III we have introduced the double-imaging technique. This section provides details on deriving recoil momentum  $p_n$  and population transfer  $\rho_{aa}$  from the imaging data.

Our atomic sample is prepared in a cross-dipole trap with slight asymmetry. When deriving the momentum transfer from the double images as in Fig. 3, we found that neither before nor after the time of flight, the absorption profile can fit perfectly to a 2D Gaussian. In addition, due to the relatively short exposure time of 20  $\mu\text{s}$  to the weak probe ( $s = 1$ ), there is substantial photon shot noise in single-shot images. To faithfully retrieve central position and atom number from each pair of double image, we take the following procedure. First, we repeat the same type of measurement for  $N = 80$  shots, and do a principal components analysis to all pairs of double images after



background subtractions. The first three components are kept for the following analysis. We then do a 2D Gaussian fit, expanding the fitted Gaussian profiles to 1.5 times the waist into a wide enough stepwise mask. The population ratios  $\rho_{aa/bb}$  are evaluated by the ratio of total counts between the two images within the mask, where the center-of-mass (c.m.) positions  $z_1$  and  $z_2$  are also directly evaluated.

We note that the first image senses atoms at  $F = 3$  “ $|a_m\rangle$ ” states only. In other words, the atoms kicked to the “visible” (or “invisible,” depending on whether the kicking number  $n$  is an even or odd number) hyperfine levels are postselected. Since there is a small interval  $\tau_{p,1}$  between SDK and the first image, there is a bias to the c.m. position  $z_1$  of the whole cloud due to this postselection. To correct for the bias, we rewrite the position difference as  $z_2 - z_1 = \tilde{v}_n \tau_{\text{TOF}} + \rho_{bb,n} \tilde{v}_{b,n} \tau_{p,1}$ . Here  $\tilde{v}_n$  and  $\tilde{v}_{b,n}$  are the mean velocity for the whole atomic ensemble and for the atoms in  $F = 2$  after  $n$  SDKs, respectively. The correction to the postselection-induced velocity bias is then given by

$$\tilde{v}_n = v_n \left( 1 - \rho_{bb,n} v_{b,n} \frac{\tau_{p,1}}{\tau_{\text{TOF}}} \right) \equiv v_n \left( 1 - \xi(n, v_n) \frac{\tau_{p,1}}{\tau_{\text{TOF}}} \right). \quad (\text{D1})$$

Here,  $\xi(n, v_n)$  depends on the relation between  $v_n$  and  $\rho_{bb,n} v_{b,n}$ . The relation can be approximated with the model in Appendix C. With  $\tau_{p,1} \sim 15 \mu\text{s}$  in our experiment, this correction is typically  $1 - \tilde{v}_n/v_n \sim \pm 5\%$  (the  $\pm$  signs depend on  $n$ ), which impacts  $f_R$  at 3% level. The correction is model dependent. We correct for the bias in our final estimation of  $f_{\text{SDK}}$  and leave 3% as the dominant uncertainty in our  $f_{\text{SDK}}$  estimation.

### APPENDIX E: IMPACT OF MIRROR OPTICAL LOSS TO $f_{\text{SDK}}$

Numerical simulations suggest that the reflectivity  $r = |\kappa|^2$  of the retroreflection mirror (Fig. 2) affects  $f_{\text{SDK}}$  at the 1% level. To investigate the effect, we sample  $0 < r < 1$  during the simulation, and calculate Raman transfer efficiency  $f_R$  and SDK fidelity  $f_{\text{SDK}}$  with peak Raman pulse area  $\mathcal{A}_R$  as in Fig. 10(a). In light of the mixed state nature of the experimental measurements, here the results are again averaged over the initial states  $|b_m\rangle$ . For all the simulation, we evaluate peak Rabi frequency  $\Omega_{a,b}$  as in previous work of electric dipole transition control [15] where the laser beam waist and the atomic ensemble size are also carefully characterized. Based on the geometry parameters, we plot the fractions of atoms as a function of peak Raman pulse area in Fig. 10(a) in histograms. The fractions are applied to weight the average over all pulse areas for the evaluation of  $\langle f_R \rangle$  and  $\langle f_{\text{SDK}} \rangle$  at various reflectivity  $r$  in Fig. 10(b). On the plot, the measured Raman transfer efficiency  $f_R$  suggest  $r \sim 55(5)\%$ . This reflectivity is

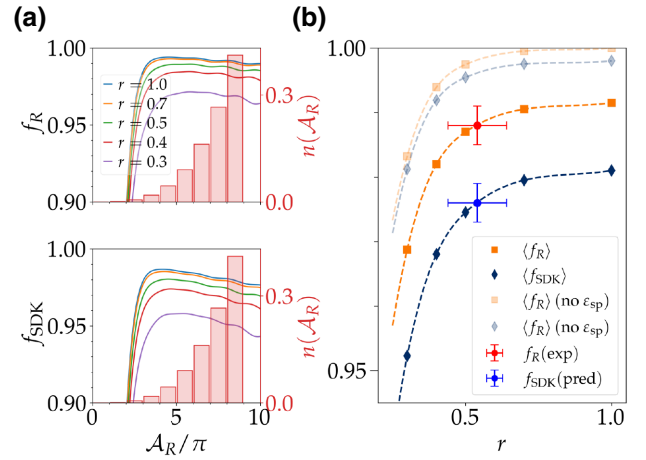


FIG. 10. (a) Numerical simulations for  $f_R$  and  $f_{\text{SDK}}$  versus Raman pulse area  $\mathcal{A}_R$  for different reflectivity  $r = |\kappa|^2$  of the retroreflection mirrors. The red bars show estimated distribution of atoms subject to different pulse areas under the Gaussian beam illumination in this experiment. (b)  $n(\mathcal{A}_R)$ -weighted average  $f_R$  and  $f_{\text{SDK}}$  versus reflectivity  $r$ . The experimentally measured  $f_R$  and inferred  $f_{\text{SDK}}$  are marked with error bars.

consistent with experimental measurements on the ratio of Stark shifts by the incident and reflected beams.

### APPENDIX F: DIFFERENT NUCLEAR SPINS

In the main text we have discussed the nanosecond SDK for  $^{85}\text{Rb}$  atoms featuring  $m = 0, \pm 1, \pm 2$  weakly coupled subspins (Fig. 1). In particular, in Sec. IV we have shown that within the experimentally explored parameter regime, a balanced chirp-alternating sequence  $\tilde{U}_{\text{uddu}}^{(4N)}(\mathbf{k}_R)$  [Eq. (11)] quite efficiently suppress the leakage among the five subspins to achieve phase gate fidelity  $\mathcal{F}_m^{(4N)} \approx 90 \sim 98\%$  at large  $N$ , for most of light intensities (Fig. 7). As clarified in Sec. IV C, the leakage suppression exploits the approximate time-reversal symmetry to cancel the nonadiabatic tunnelings among the subspins. Practically, the leakage dynamics supported by the nondegenerate subspins is complex enough to merit future study by itself. Instead of attempting a full understanding of the dynamics, in this section we provide numerical examples of coherent matterwave control for other alkaline species. The simulations are according to those outlined in Appendix B and in parallel to Fig. 7, in particular with spontaneous emission ignored by setting  $\Gamma_e = 0$  on the D1 line. The examples with nuclear spin  $I = 1.5, 2.5, 3.5$  are given in Figs. 11, 12, 13, respectively. To compare with the Fig. 7 results, we set the hyperfine splittings  $\omega_{\text{HFS},g}, \omega_{\text{HFS},e}$  to be identical to  $^{85}\text{Rb}$  for all the simulations. In addition, we choose  $\Delta_e = -6.6\omega_{\text{HFS},g}$ , twice as those for Fig. 7, to demonstrate the substantially enhanced spin-leakage suppression.

Figure 11 compares the SDK phase gate fidelity by the traditional  $\tilde{U}_{\text{uu}}^{(4N)}$  (left) and the chirp-alternating  $\tilde{U}_{\text{uddu}}^{(4N)}$

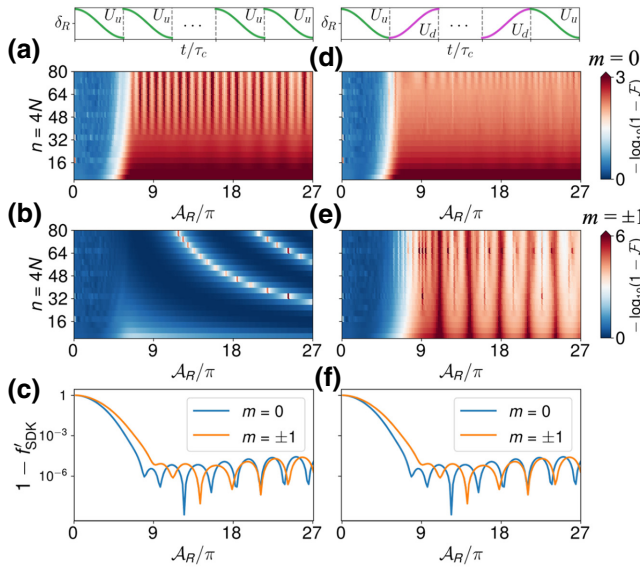


FIG. 11. Numerical results of gate infidelity  $1 - \mathcal{F}$  for the traditional  $\tilde{U}_{uu}^{(4N)}$  (left panels) and balanced chirp-alternating  $\tilde{U}_{uddu}^{(4N)}$  (right panels) controls as those in Fig. 7,  $\mathcal{F} = \mathcal{F}_m^{(4N)}$ , except for  $\Delta = -6.6\omega_{\text{HFS,g}}$  here and for a fictitious  $^{85}\text{Rb}$  atom with nuclear spin  $I = 1.5$ . The two-photon detuning profiles are illustrated on top of (a),(d). The exceptionally high fidelity demonstrated in (e) is a result of  $m = \pm 1$  subspin degeneracy in the Raman control dynamics. For comparison,  $1 - f'_{\text{SDK}}$  for a single kick is plotted in both (c),(f) by setting  $\Delta_{\text{HFS,e}} = 0$  to suppress the spin leakage according to Eq. (1).

(right) sequences, for the  $^{87}\text{Rb}$ -like atom. With  $F_b = 1$  for  $I = 1.5$  [Fig. 1(a)], there are three subspins with  $m = 0, \pm 1$ . The  $m = 0$  subspin is only coupled to single  $|a_m\rangle$  states with  $m = \pm 2$  [similar to the  $m = \pm 3$  end couplings in Fig. 1(a)]. The gate infidelity for  $\tilde{U}_{uu}^{(4N)}$  is slightly compromised by the resulting leakage ( $\mathcal{F}_m^{(4N)}$ ) between 98.5% and 99.9% at  $4N = 80$ , as in Fig. 11(a). For comparison, in absence subspin leakage to fix, the gate fidelity for the chirp-alternating  $\tilde{U}_{uddu}^{(4N)}$  in Fig. 11(d) is even slightly worse ( $\mathcal{F}_m^{(4N)}$ ) between 98.5% and 99.5% at  $4N = 80$ . Nevertheless, we note the  $\tilde{U}_{uddu}^{(4N)}$  is still preferred practically, not only because it supports the  $m = \pm 1$  subspin performance to be discussed next, but also due to the robust dynamic phase cancellation (Sec. IV D).

In contrast, the resonant leakages between the degenerate  $m = \pm 1$  subspins is substantial, which strongly affect the gate fidelity for  $\tilde{U}_{uu}^{(4N)}$ . This is shown in Fig. 11(b) similar to the Fig. 7(b) results. Interestingly, in the absence of the  $m = \pm 3$  end couplings for  $^{85}\text{Rb}$  [Fig. 1(a)], here the leakage suppression by chirp alternating the  $\tilde{U}_{uddu}^{(4N)}$  sequence is essentially perfect for the  $^{87}\text{Rb}$ -like atom. As in Fig. 11(e), the  $\mathcal{F}_m^{(4N)}$  reaches 99.99% level at large  $N$ , which appears to be only limited by the  $\text{SU}(2)$  nonadiabaticity of single adiabatic SDK [58], as suggested by  $f'_{\text{SDK}}$  in Figs. 11(c), 11(f) evaluated according to Eq. (6), after

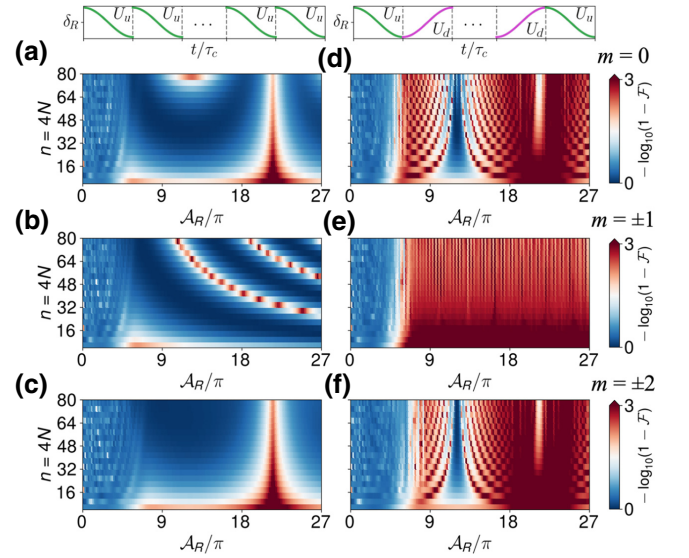


FIG. 12. Numerical results of gate infidelity  $1 - \mathcal{F}$  for the traditional  $\tilde{U}_{uu}^{(4N)}$  (left panels) and balanced chirp-alternating  $\tilde{U}_{uddu}^{(4N)}$  (right panels) controls as those in Fig. 7,  $\mathcal{F} = \mathcal{F}_m^{(4N)}$ , except for  $\Delta = -6.6\omega_{\text{HFS,g}}$  here. The corresponding two-photon detuning profiles are illustrated on top of (a),(d).

setting  $\omega_{\text{HFS,e}} = 0$  to remove the  $m$ -changing couplings [Eq. (1)].

Next, Fig. 12 investigates SDK phase gate fidelity for  $^{85}\text{Rb}$  featuring five nearly degenerate subspins with  $m = 0, \pm 1, \pm 2$ , as in the main text. Here the single-photon detuning  $\Delta_e = -6.6\omega_{\text{HFS,g}}$  is doubled to be compared with the Fig. 7 results. We see that for both  $\tilde{U}_{uu}^{(4N)}$  and  $\tilde{U}_{uddu}^{(4N)}$  sequences, at the larger  $\Delta_e$  the intensity-dependent  $\mathcal{F}_m^{(4N)}$  oscillatory features due to the spin leakages are slowed (with respect to the increasing  $n = 4N$ ) and sharpened. With the  $\Omega^{\pm 2}$  couplings halved [Eq. (1)] relative to the Fig. 7 case, the infidelity for the  $\tilde{U}_{uddu}^{(4N)}$  sequence is now below 1% at the large  $N$ , for most of the large laser intensities. The low- $\mathcal{F}$  region is now narrowed within  $11 < A_R/\pi < 13$ .

Finally, Fig. 13 investigates SDK phase gate fidelity for  $^{133}\text{Cs}$ -like atom featuring seven nearly degenerate subspins with  $m = 0, \pm 1, \pm 2, \pm 3$ . With the large number of subspins involved, the spin-leakage dynamics are more complex. Nevertheless, comparing with the gate fidelity for  $\tilde{U}_{uu}^{(4N)}$  in Figs. 13(a)–13(d), in Figs. 13(e)–13(h) the drastic fidelity enhancement due to the spin-leakage suppression by  $\tilde{U}_{uddu}^{(4N)}$  is evident. For the seven subspin system, the strips of the low- $\mathcal{F}$  intensity region become quite widely distributed. Consequently, comparing to the  $^{87}\text{Rb}$ -like atom with Figs. 11(d) and 11(e) and the  $^{85}\text{Rb}$ -like atom with Figs. 12(d)–12(f), it becomes more difficult to find a suitable range of laser intensities for the high-fidelity multi- $m$  SDK phase gates to operate. More generally, as the nuclear spin  $I$  increases, it becomes more difficult to

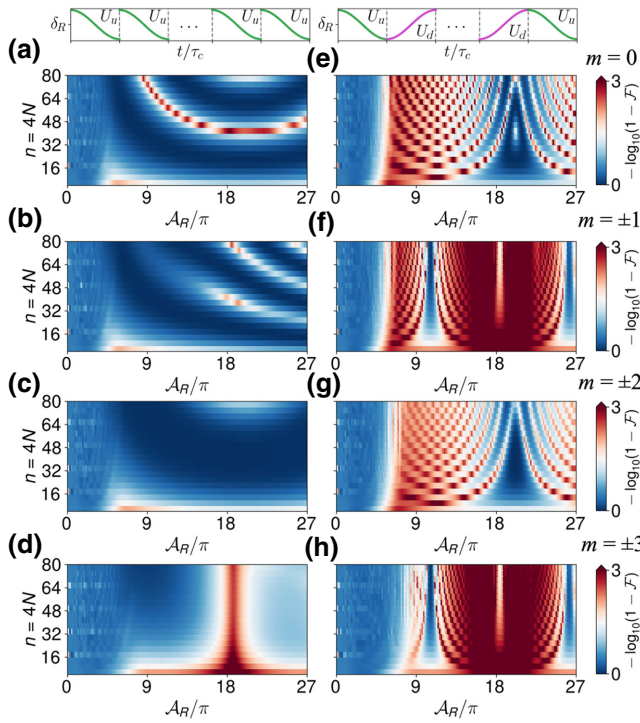


FIG. 13. Numerical results of gate infidelity  $1 - \mathcal{F}$  for the traditional  $\tilde{U}_{uu}^{(4N)}$  (left panels) and balanced chirp-alternating  $\tilde{U}_{uudu}^{(4N)}$  (right panels) controls as those in Fig. 7,  $\mathcal{F} = \mathcal{F}_m^{(4N)}$ , except for  $\Delta = -6.6\omega_{\text{HFS},g}$  here and for a fictitious  $^{85}\text{Rb}$  atom with nuclear spin  $I = 3.5$ . The corresponding two-photon detuning profiles are illustrated on top of (a),(e).

achieve  $m$ -independent phase gate prescribed by Eq. (8) in the main text with composite SDK. To improve the aspect, variations of additional pulse parameters beyond the simple chirp alternation as in this work may be explored. In addition, in measurements where coherent control of a single  $m$ -spinor matterwave, such as the  $m = 0$  clock states, is all that is needed, then circularly polarized nanosecond pulses can be applied to naturally suppress the  $m$ -changing transitions during the spinor matterwave control [69]. To this end, we expect the delay-line-based nanosecond SDK to facilitate the accurate implementation of  $m$ -preserving Raman control with circularly polarized pulses [61].

[1] M. Kasevich and S. Chu, Atomic Interferometry Using Stimulated Raman Transitions, *Phys. Rev. Lett.* **67**, 181 (1991).  
 [2] P. D. Featonby, G. S. Summy, J. L. Martin, H. Wu, K. P. Zetie, C. J. Foot, and K. Burnett, Adiabatic transfer for atomic interferometry, *Phys. Rev. A* **53**, 373 (1996).  
 [3] J. M. McGuirk, M. J. Snadden, and M. A. Kasevich, Large Area Light-Pulse Atom Interferometry, *Phys. Rev. Lett.* **85**, 4498 (2000).  
 [4] H. J. Metcalf and P. van der Straten, *Laser Cooling and Trapping* (Springer-Verlag, New York, 1999).

[5] J. Mizrahi, C. Senko, B. Neyenhuis, K. G. Johnson, W. C. Campbell, C. W. S. Conover, and C. Monroe, Ultrafast Spin-Motion Entanglement and Interferometry with a Single Atom, *Phys. Rev. Lett.* **110**, 203001 (2013).  
 [6] M. Jaffe, V. Xu, P. Haslinger, H. Müller, and P. Hamilton, Efficient Adiabatic Spin-Dependent Kicks in an Atom Interferometer, *Phys. Rev. Lett.* **121**, 040402 (2018).  
 [7] T. P. Harty, D. T. C. Allcock, C. J. Ballance, L. Guidoni, H. A. Janacek, N. M. Linke, D. N. Stacey, and D. M. Lucas, High-Fidelity Preparation, Gates, Memory, and Readout of a Trapped-Ion Quantum Bit, *Phys. Rev. Lett.* **113**, 220501 (2014).  
 [8] C. J. Ballance, T. P. Harty, N. M. Linke, M. A. Sepiol, and D. M. Lucas, High-Fidelity Quantum Logic Gates Using Trapped-Ion Hyperfine Qubits, *Phys. Rev. Lett.* **117**, 060504 (2016).  
 [9] Y. Wang, A. Kumar, T.-Y. Wu, and D. S. Weiss, Single-qubit gates based on targeted phase shifts in a 3D neutral atom array, *Science* **352**, 1562 (2016).  
 [10] K. Kotru, D. L. Butts, J. M. Kinast, and R. E. Stoner, Large-Area Atom Interferometry with Frequency-Swept Raman Adiabatic Passage, *Phys. Rev. Lett.* **115**, 103001 (2015).  
 [11] J. J. García-Ripoll, P. Zoller, and J. I. Cirac, Speed Optimized Two-Qubit Gates with Laser Coherent Control Techniques for Ion Trap Quantum Computing, *Phys. Rev. Lett.* **91**, 157901 (2003).  
 [12] L. M. Duan, Scaling Ion Trap Quantum Computation through Fast Quantum Gates, *Phys. Rev. Lett.* **93**, 100502 (2004).  
 [13] H. Y. Lo, D. Kienzler, L. De Clercq, M. Marinelli, V. Negnevitsky, B. C. Keitch, and J. P. Home, Spin-motion entanglement and state diagnosis with squeezed oscillator wavepackets, *Nature* **521**, 336 (2015).  
 [14] Y. Ma, X. Huang, X. Wang, L. Ji, Y. He, L. Qiu, J. Zhao, Y. Wang, and S. Wu, Precise pulse shaping for quantum control of strong optical transitions, *Opt. Express* **28**, 17171 (2020).  
 [15] Y. He, L. Ji, Y. Wang, L. Qiu, J. Zhao, Y. Ma, X. Huang, S. Wu, and D. E. Chang, Atomic spin-wave control and spin-dependent kicks with shaped subnanosecond pulses, *Phys. Rev. Res.* **2**, 043418 (2020).  
 [16] V. M. Schäfer, C. J. Ballance, K. Thirumalai, L. J. Stephenson, T. G. Ballance, A. M. Steane, and D. M. Lucas, Fast quantum logic gates with trapped-ion qubits, *Nature* **555**, 75 (2018).  
 [17] C. Flühmann, T. L. Nguyen, M. Marinelli, V. Negnevitsky, K. Mehta, and J. P. Home, Encoding a qubit in a trapped-ion mechanical oscillator, *Nature* **566**, 513 (2019).  
 [18] S. S. Szigeti, S. P. Nolan, J. D. Close, and S. A. Haine, High-Precision Quantum-Enhanced Gravimetry with a Bose-Einstein Condensate, *Phys. Rev. Lett.* **125**, 100402 (2020).  
 [19] Y. Wu, R. Krishnakumar, J. Martínez-Rincón, B. K. Malia, O. Hosten, and M. A. Kasevich, Retrieval of cavity-generated atomic spin squeezing after free-space release, *Phys. Rev. A* **102**, 012224 (2020).  
 [20] F. Anders, A. Idel, P. Feldmann, D. Bondarenko, S. Loriani, K. Lange, J. Peise, M. Gersemann, B. Meyer-Hoppe, S. Abend, N. Gaaloul, C. Schubert, D. Schlippert, L. Santos, E. Rasel, and C. Klempt, Momentum Entanglement for Atom Interferometry, *Phys. Rev. Lett.* **127**, 140402 (2021).

- [21] G. P. Greve, C. Luo, B. Wu, and J. K. Thompson, [arXiv:2110.14027](https://arxiv.org/abs/2110.14027) (2021).
- [22] G. T. Genov, D. Schraft, T. Halfmann, and N. V. Vitanov, Correction of Arbitrary Field Errors in Population Inversion of Quantum Systems by Universal Composite Pulses, *Phys. Rev. Lett.* **113**, 043001 (2014).
- [23] G. H. Low, T. J. Yoder, and I. L. Chuang, Methodology of Resonant Equiangular Composite Quantum Gates, *Phys. Rev. X* **6**, 041067 (2016).
- [24] J. C. Saywell, I. Kuprov, D. Goodwin, M. Carey, and T. Freearge, Optimal control of mirror pulses for cold-atom interferometry, *Phys. Rev. A* **98**, 023620 (2018).
- [25] D. S. Weiss, B. C. Young, and S. Chu, Precision measurement of  $\hbar/m_Cs$  based on photon recoil using laser-cooled atoms and atomic interferometry, *Appl. Phys. B* **59**, 217 (1994).
- [26] W. Happer, Optical pumping, *Rev. Mod. Phys.* **44**, 169 (1972).
- [27] M. Kasevich and S. Chu, Measurement of the gravitational acceleration of an atom with a light-pulse atom interferometer, *Appl. Phys. B* **54**, 321 (1992).
- [28] D. S. Durfee, Y. K. Shaham, and M. A. Kasevich, Long-Term Stability of an Area-Reversible Atom-Interferometer Sagnac Gyroscope, *Phys. Rev. Lett.* **97**, 240801 (2006).
- [29] B. Canuel, F. Leduc, D. Holleville, A. Gauguier, J. Fils, A. Viridis, A. Clairon, N. Dimarcq, C. J. Bordé, A. Landragin, and P. Bouyer, Six-Axis Inertial Sensor Using Cold-Atom Interferometry, *Phys. Rev. Lett.* **97**, 010402 (2006).
- [30] N. Malossi, Q. Bodart, S. Merlet, A. Landragin, F. P. D. Santos, and O. D. Paris, Double diffraction in an atomic gravimeter, *Phys. Rev. A* **81**, 013617 (2009).
- [31] L. Zhou, S. Long, B. Tang, X. Chen, F. Gao, W. Peng, W. Duan, J. Zhong, Z. Xiong, J. Wang, Y. Zhang, and M. Zhan, Test of Equivalence Principle at  $10^{-8}$  Level by a Dual-Species Double-Diffraction Raman Atom Interferometer, *Phys. Rev. Lett.* **115**, 013004 (2015).
- [32] I. Perrin, J. Bernard, Y. Bidel, A. Bonnin, N. Zahzam, C. Blanchard, A. Bresson, and M. Cadoret, Zero-velocity atom interferometry using a retroreflected frequency-chirped laser, *Phys. Rev. A* **100**, 053618 (2019).
- [33] S. Hartmann, J. Jenewein, E. Giese, S. Abend, A. Roura, E. M. Rasel, and W. P. Schleich, Regimes of atomic diffraction: Raman versus Bragg diffraction in retroreflective geometries, *Phys. Rev. A* **101**, 53610 (2020).
- [34] A. Peters, K. Y. Chung, B. Young, J. Hensley, and S. Chu, Precision atom interferometry, *Phil. Trans. R. Soc. Lond. A* **355**, 2223 (1997).
- [35] P. Kral, I. Thanopoulos, and M. Shapiro, Colloquium: Coherently controlled adiabatic passage, *Rev. Mod. Phys.* **79**, 53 (2007).
- [36] Y. He, L. Ji, Y. Wang, L. Qiu, J. Zhao, Y. Ma, X. Huang, S. Wu, and D. E. Chang, Geometric Control of Collective Spontaneous Emission, *Phys. Rev. Lett.* **125**, 213602 (2020).
- [37] B. Estey, C. Yu, and H. Müller, High-Resolution Atom Interferometers with Suppressed Diffraction Phases, *Phys. Rev. Lett.* **115**, 083002 (2015).
- [38] S. L. Kristensen, M. Jaffé, V. Xu, C. D. Panda, and H. Müller, Raman transitions driven by phase-modulated light in a cavity atom interferometer, *Phys. Rev. A* **103**, 023715 (2021).
- [39] J. Mizrahi, B. Neyenhuis, K. G. Johnson, W. C. Campbell, C. Senko, D. Hayes, and C. Monroe, Quantum control of qubits and atomic motion using ultrafast laser pulses, *Appl. Phys. B* **114**, 45 (2014).
- [40] D. Stack, J. Elgin, P. M. Anisimov, and H. Metcalf, Numerical studies of optical forces from adiabatic rapid passage, *Phys. Rev. A* **013420**, 013420 (2011).
- [41] D. J. Wineland, M. Barrett, J. Britton, J. Chiaverini, B. DeMarco, W. M. Itano, B. Jelenkovic, C. Langer, D. Leibfried, V. Meyer, T. Rosenband, and T. Schatz, Quantum information processing with trapped ions, *Phil. Trans. R. Soc. Lond. A* **361**, 1349 (2003).
- [42] B. Plotkin-Swing, D. Gochnauer, K. E. McAlpine, E. S. Cooper, A. O. Jamison, and S. Gupta, Three-Path Atom Interferometry with Large Momentum Separation, *Phys. Rev. Lett.* **121**, 133201 (2018).
- [43] P. Asenbaum, C. Overstreet, M. Kim, J. Curti, and M. A. Kasevich, Atom-Interferometric Test of the Equivalence Principle at the  $10^{-12}$  Level, *Phys. Rev. Lett.* **125**, 191101 (2020).
- [44] H. Müller, S. W. Chiow, S. Herrmann, and S. Chu, Atom Interferometers with Scalable Enclosed Area, *Phys. Rev. Lett.* **102**, 240403 (2009).
- [45] M. Gebbe, J. N. Siemß, M. Gersemann, H. Müntinga, S. Herrmann, C. Lämmerzahl, H. Ahlers, N. Gaaloul, C. Schubert, K. Hammerer, S. Abend, and E. M. Rasel, Twin-lattice atom interferometry, *Nat. Commun.* **12**, 2544 (2021).
- [46] J. Rudolph, T. Wilkason, M. Nantel, H. Swan, C. M. Holland, Y. Jiang, B. E. Garber, S. P. Carman, and J. M. Hogan, Large Momentum Transfer Clock Atom Interferometry on the 689 nm Intercombination Line of Strontium, *Phys. Rev. Lett.* **124**, 83604 (2020).
- [47] T. Wilkason, M. Nantel, J. Rudolph, Y. Jiang, B. E. Garber, H. Swan, S. P. Carman, M. Abe, and J. M. Hogan, [arXiv:2205.06965](https://arxiv.org/abs/2205.06965) (2022).
- [48] D. A. Steck, (2016), available online at <http://steck.us/teaching> (revision 0.11.5, 27 November 2016).
- [49] A. Dunning, R. Gregory, J. Bateman, N. Cooper, M. Himsforth, J. A. Jones, and T. Freearge, Composite pulses for interferometry in a thermal cold atom cloud, *Phys. Rev. A* **90**, 033608 (2014).
- [50] A. Cidrim, A. P. Orioli, C. Sanner, R. B. Hutson, J. Ye, R. Bachelard, and A. M. Rey, Dipole-Dipole Frequency Shifts in Multilevel Atoms, *Phys. Rev. Lett.* **127**, 013401 (2021).
- [51] R. Delhuille, A. Miffre, C. Robilliard, J. Vigue, M. Bu, and C. Champenois, Diffraction phases in atom interferometers, *Phys. Rev. A* **68**, 013607 (2003).
- [52] E. Magesan, J. M. Gambetta, and J. Emerson, Characterizing quantum gates via randomized benchmarking, *Phys. Rev. A - At. Mol. Opt. Phys.* **85**, 042311 (2012).
- [53] J. Dalibard, Y. Castin, and K. Molmer, Wave-Function Approach to Dissipative Processes in Quantum Optics, *Phys. Rev. Lett.* **68**, 580 (1992).
- [54] H. J. Carmichael, *Lecture Notes in Physics*, New Series m: Monographs (Springer, Berlin, 1993), Vol. m18.
- [55] K. Bergmann, H. Theuer, and B. W. Shore, Coherent population transfer among quantum states of atoms and molecules, *Rev. Mod. Phys.* **70**, 1003 (1998).

- [56] N. V. Vitanov, T. Halfmann, B. W. Shore, and K. Bergmann, Laser-induced population transfer by adiabatic passage techniques, *Annu. Rev. Phys. Chem.* **52**, 763 (2001).
- [57] X. Miao, E. Wertz, M. G. Cohen, and H. Metcalf, Strong Optical Forces from Adiabatic Rapid Passage, *Phys. Rev. Lett.* **75**, 011402 (2007).
- [58] D. Guery-Odelin, A. Ruschhaupt, A. Kiely, E. Torrontegui, S. Martínez-Garaot, and J. G. Muga, Shortcuts to adiabaticity: Concepts, methods, and applications, *Rev. Mod. Phys.* **91**, 045001 (2019).
- [59] M. V. Berry, Quantal phase factors accompanying adiabatic changes, *Proc. R. Soc. London. A. Math. Phys. Sci.* **392**, 45 (1984).
- [60] S.-I. Zhu and Z. D. Wang, Implementation of Universal Quantum Gates Based on Nonadiabatic Geometric Phases, *Phys. Rev. Lett.* **89**, 097902 (2002).
- [61] T. L. Gustavson, Ph.D. thesis, Stanford University, 2000.
- [62] T. Lu, X. Miao, and H. Metcalf, Bloch theorem on the Bloch sphere, *Phys. Rev. A* **71**, 061405 (2005).
- [63] F. Sievers, N. Kretzschmar, D. Fernandes, D. Suchet, M. Rabinovic, S. Wu, C. Parker, L. Khaykovich, C. Salomon, and F. Chevy, Simultaneous sub-Doppler laser cooling of fermionic  ${}^6\text{Li}$  and  ${}^{40}\text{K}$  on the  $D_1$  line: Theory and experiment, *Phys. Rev. A - At. Mol. Opt. Phys.* **91**, 023426 (2015).
- [64] G. T. Genov and N. V. Vitanov, Dynamical Suppression of Unwanted Transitions in Multistate Quantum Systems, *Phys. Rev. Lett.* **110**, 133002 (2013).
- [65] Y. H. Kang, Y. H. Chen, Z. C. Shi, B. H. Huang, J. Song, and Y. Xia, Pulse design for multilevel systems by utilizing Lie transforms, *Phys. Rev. A* **97**, 033407 (2018).
- [66] H. Jo, Y. Song, and J. Ahn, Qubit leakage suppression by ultrafast composite pulses, *Opt. Express* **27**, 3944 (2019).
- [67] B. W. Shore, Two-state behavior in  $N$ -state quantum systems: The Morris-Shore transformation reviewed, *J. Mod. Opt.* **61**, 787 (2014).
- [68] J. A. Muniz, M. A. Norcia, J. R. K. Cline, and J. K. Thompson, [arXiv:1806.00838](https://arxiv.org/abs/1806.00838) (2018).
- [69] It is worth pointing out that the  $\Delta m \neq 0$  spin leakage is naturally suppressed when Raman transitions are driven by beams with the same circular polarization [61]. Here, circularly polarized nanosecond SDK can be implemented on a compact delay line. When combined with the balanced chirp-alternating scheme, coherent control of a specific Zeeman spinor matterwave component can be achieved with robustly cancelled dynamic phases. However, since both the two-photon shift and the Raman Rabi frequency of the circular polarized SDK are highly  $m$  dependent, it would be more difficult to achieve the parallel multi-Zeeman spinor control.
- [70] A. Bertoldi, F. Minardi, and M. Prevedelli, Phase shift in atom interferometers: Corrections for nonquadratic potentials and finite-duration laser pulses, *Phys. Rev. A* **99**, 033619 (2019).
- [71] In atom interferometry, the  $R_\varphi(\theta)$  operations are usually achieved with simple Raman pulses with little resilience to control errors. Methods for error-resilience realization of  $R_\varphi(\theta)$  are discussed in, e.g., Ref. [24]. Similarly, we find  $R_\varphi(\theta)$  can be achieved with composite pulses. The results will be presented in a future publication.
- [72] L. A. Sidorenkov, R. Gautier, M. Altorio, R. Geiger, and A. Landragin, Tailoring Multiloop Atom Interferometers with Adjustable Momentum Transfer, *Phys. Rev. Lett.* **125**, 213201 (2020).
- [73] B. Dubetsky and M. A. Kasevich, Atom interferometer as a selective sensor of rotation or gravity, *Phys. Rev. A - At. Mol. Opt. Phys.* **74**, 023615 (2006).
- [74] C. Petitjean, D. V. Bevilacqua, E. J. Heller, and P. Jacquod, Displacement Echoes: Classical Decay and Quantum Freeze, *Phys. Rev. Lett.* **98**, 164101 (2007).
- [75] E. Su, S. Wu, and M. Prentiss, Atom interferometry using wave packets with constant spatial displacements, *Phys. Rev. A - At. Mol. Opt. Phys.* **81**, 043631 (2010).
- [76] The projected interferometry performance is subtly enhanced by the time-reversal symmetry of the interferometry itself, introduced by the  $R_2$  rotation. Practically, the symmetry can be broken by atomic motion during the long interrogation time  $T$ . In this case, the high-level performance can still be retained by avoiding the narrow low- $\mathcal{F}$  intensity regions in all the SDK sequences.
- [77] C. Gross and I. Bloch, Quantum simulations with ultracold atoms in optical lattices, *Science* **357**, 995 (2017).
- [78] R. Blatt and C. F. Roos, Quantum simulations with trapped ions, *Nat. Phys.* **8**, 277 (2012).
- [79] Y.-J. Wang, D. Anderson, V. Bright, E. Cornell, Q. Diot, T. Kishimoto, M. Prentiss, R. Saravanan, S. Segal, and S. Wu, Atom Michelson Interferometer on a Chip Using a Bose-Einstein Condensate, *Phys. Rev. Lett.* **94**, 090405 (2005).
- [80] K. J. Hughes, J. H. Burke, and C. A. Sackett, Suspension of Atoms Using Optical Pulses, and Application to Gravimetry, *Phys. Rev. Lett.* **102**, 150403 (2009).
- [81] J. E. Debs, P. A. Altin, T. H. Barter, D. Döring, G. R. Dennis, G. McDonald, R. P. Anderson, J. D. Close, and N. P. Robins, Cold-atom gravimetry with a Bose-Einstein condensate, *Phys. Rev. A - At. Mol. Opt. Phys.* **84**, 033610 (2011).
- [82] S. Abend, M. Gebbe, M. Gersemann, H. Ahlers, H. Müntinga, E. Giese, N. Gaaloul, C. Schubert, C. Lämmerzahl, W. Ertmer, W. P. Schleich, and E. M. Rasel, Atom-Chip Fountain Gravimeter, *Phys. Rev. Lett.* **117**, 203003 (2016).
- [83] C. D. Macrae, K. Bongs, and M. Holynski, Optical frequency generation using fiber Bragg grating filters for applications in portable quantum sensing, *Opt. Lett.* **46**, 1257 (2021).
- [84] Y. Wang, Y. He, L. Ji, J. Hu, X. Huang, Y. Ma, L. Qiu, K. Zhao, and S. Wu, Intense, wideband optical waveform generation by self-balanced amplification of fiber electro-optical sideband modulation, *Chinese Opt. Lett.* **20**, 111401 (2022).
- [85] A. M. Jayich, A. C. Vutha, M. T. Hummon, J. V. Porto, and W. C. Campbell, Continuous all-optical deceleration and single-photon cooling of molecular beams, *Phys. Rev. A* **89**, 023425 (2014).
- [86] R. Liu, Y. Ma, L. Ji, L. Qiu, M. Ji, Z. Tao, and S. Wu, Composite acousto-optical modulation, *Opt. Express* **30**, 27780 (2022).

- [87] G. D. Bruce, E. Haller, B. Peaudecerf, D. A. Cotta, M. Andia, S. Wu, M. Y. H. Johnson, B. W. Lovett, and S. Kuhr, Sub-Doppler laser cooling of  $^{40}\text{K}$  with Raman gray molasses on the  $D_2$  line, *J. Phys. B: At. Mol. Opt. Phys* **50**, 095002 (2017).
- [88] R. Dum, A. S. Parkins, P. Zoller, and C. W. Gardiner, Monte Carlo simulation of master equations in quantum optics for vacuum, thermal, and squeezed reservoirs, *Physical Rev. A* **46**, 4382 (1992).